The role of nearshore air-sea interactions for landfalling atmospheric rivers on the U.S. West Coast

Samuel T. Bartusek[1,2], Hyodae Seo[2], Caroline C. Ummenhofer[2], John Steffen[2]

[1]Department of Geosciences, Princeton University

[2]Department of Physical Oceanography, Woods Hole Oceanographic Institution

Corresponding author: Samuel T. Bartusek (samueltb@princeton.edu)

Key Points

- Atmospheric Rivers (ARs) experience upward latent heat flux (LHF) over the coastal ocean, strongest 1–3 days before and after landfall.
- In El Niño winters, LHF during ARs is enhanced along the southern coast and reduced along the northern coast by ~70% relative to La Niña.
- LHF decomposition reveals sea surface temperature variability via ENSO as a dominant contributor to interannual coastal LHF variations.

Abstract

Research on Atmospheric Rivers (ARs) has focused primarily on AR (thermo)dynamics and hydrological impacts over land. However, the evolution and potential role of nearshore air-sea fluxes during landfalling ARs are not well documented. Here, we examine synoptic evolutions of nearshore latent heat flux (LHF) during strong late-winter landfalling ARs (1979–2017) using 138 over-shelf buoys along the U. S. west coast. Composite evolutions show that ARs typically receive upward (absolute) LHF from the coastal ocean. LHF is small during landfall due to weak air-sea humidity gradients but is strongest (30–50 W/m^2 along the coast) 1–3 days before/after landfall. During El Niño winters, southern-coastal LHF strengthens, coincident with stronger ARs. A decomposition of LHF reveals that sea surface temperature (SST) anomalies modulated by the El Niño—Southern Oscillation dominate interannual LHF variations under ARs, suggesting a potential role for nearshore SST and LHF influencing the intensity of landfalling ARs.

Plain Language Summary

Atmospheric Rivers (ARs) are elongated streams of enhanced water vapor transport, contributing to a substantial fraction of total wintertime precipitation and extreme streamflow events along the U.S. west coast. Thus, better understanding the processes contributing to the intensity of landfalling ARs is of broad scientific and societal interests. Considerable efforts have been directed at their meteorological structures and hydrological impacts over land, but it remains unclear if and how the severity of landfalling ARs is influenced by their interactions with coastal oceans. Here, we use *in situ* near-surface atmospheric and sea surface temperature measurements from 138 over-shelf buoys along the U.S. west coast to characterize variations of latent heat flux during strong late-winter landfalling ARs from 1979 to 2017. We find that the coastal ocean is an important heat and moisture source for ARs in the days before landfall. During El Niño events, the oceanic heat and moisture input to the atmosphere increases along the southern coast, coincident with more intense ARs. Further analysis shows that surface ocean temperature anomalies related to El Niño—Southern Oscillation dominantly affect latent heat flux during landfalling ARs. Our results suggest a potential role for the coastal ocean in influencing the intensity of landfalling ARs.

Index Terms

4504 Air/sea interactions (0312, 3339); 4522 ENSO (4922); 4546 Nearshore processes; 3339 Ocean/atmosphere interactions (0312, 4301, 4504); 4217 Coastal processes

Keywords

Air-sea interaction; atmospheric rivers; latent heat flux; hydroclimate; U.S. west coast; coastal oceans

1. Introduction

Atmospheric Rivers (ARs) are elongated and filamentary (typically >2000 km long, <1000 km wide) plumes of enhanced atmospheric water vapor content and transport, extending from the tropics toward the midlatitudes (e.g., Zhu and Newell, 1998; Ralph et al., 2004; Neiman et al., 2008; Lavers et al., 2011). Despite their small spatial footprint and short lifetime (Ralph et al., 2004, 2013), ARs achieve >90% of poleward moisture flux in the extratropics (Zhu and Newell, 1998) due to their high vapor transport. ARs play a vital role in the global hydrological cycle (e.g., Algarra et al., 2020).

ARs are particularly critical to hydroclimate variability and the water cycle in the western U.S. ARs deliver up to half of the water-year's precipitation and regional water resources (Guan et al., 2010; Dettinger et al., 2011; Gershunov et al., 2017) and have helped alleviate or terminate 30–70% of the region's dry spells and droughts (Moore et al., 2012; Dettinger, 2013). However, the region is also vulnerable to hazards from ARs' intense precipitation. Nearly all extreme streamflow events and flooding are associated with ARs (Ralph et al., 2005, 2006, 2011; Leung and Qian, 2009; Smith et al., 2010; Dettinger et al., 2011, 2012; Ralph and Dettinger, 2012; White et al., 2012; Rutz et al., 2014). Therefore, better understanding the processes contributing to the intensity of landfalling ARs is of broad scientific and economic interests (Ralph et al., 2019a; Corringham et al., 2019).

Despite extensive research into atmospheric dynamics (e.g., Payne and Magnusdottir, 2014; Zhang et al., 2019) and hydrological impacts (e.g., Ralph et al., 2006; Neiman et al., 2011) of ARs, the behavior of nearshore air-sea fluxes during landfalling ARs remains not well

78 understood. As ARs approach the west coast, they traverse the coastal ocean, where substantial
79 coastally-trapped variability in upper ocean heat content and sea surface temperature (SST)
80 influence the magnitude of air-sea fluxes on subseasonal to interannual time-scales. For example,
81 a sustained network of glider observations (e.g., Todd et al., 2011) revealed substantial (±3-4ºC)
82 nearshore SST and heat content anomalies along the U.S. west coast associated with the El
83 Niño—Southern Oscillation (ENSO). Persson et al. (2005) provided a case study of a landfalling
84 AR resulting in widespread flooding in southern California in the winter of 1998, a strong El
85 Niño year, in which localized deep convection was ascribed to enhanced latent heat flux (LHF)
86 over this anomalously high SST. Furthermore, Gonzales et al. (2019) find that coastal SSTs
87 influence AR landfall temperatures more strongly than along-track SSTs, and Chen and Leung
88 (2020) provided modeling evidence that local SST warming significantly enhances AR intensity
89 and precipitation, likely by increasing boundary layer instability and convective available
90 potential energy (CAPE). However, it remains an open question whether enhanced SST
91 variability in the coastal oceans associated with ENSO systematically influences air-sea moisture
92 flux under landfalling ARs.
93
94 Here, we provide *in situ* information about synoptic LHF evolution during strong late-winter
95 ARs (1979–2017) landfalling along the U.S. west coast. Given the strong impact of ENSO on
96 west coast SST and precipitation (Jong et al., 2016), we further investigate the ENSO-related
97 variability of LHF, its constituent variables via flux decomposition, and AR intensity.
98
99 ARs generally represent a nearly-saturated air-mass over the cooler coastal waters, incurring
100 reduced moisture exchanges as they approach the shore. This was demonstrated by Shinoda et al.
101 (2019), who constructed composite AR evolutions based on the 1°-resolution OAFLUX dataset
102 (Yu et al., 2007), finding strong LHF anomalies upstream (far offshore) becoming small
103 downstream (nearshore). Noting the transient nature of ARs and narrow spatial extent of the
104 coastal shelf, in addition to challenges in satellite remote sensing of coastal meteorology and air-
105 sea fluxes (Cronin et al., 2019), however, analysis is necessary based on *in situ* measurements
106 that are designed for monitoring coastal processes to reinforce their finding. The authors also
107 concluded that strong ARs typically correspond with negative heat flux anomaly near the coast.
108 As we will show, despite this negative LHF anomaly, the absolute magnitude of LHF remains

109 positive, indicating that the coastal ocean provides moisture and heat to ARs, potentially
110 affecting their intensity.
111

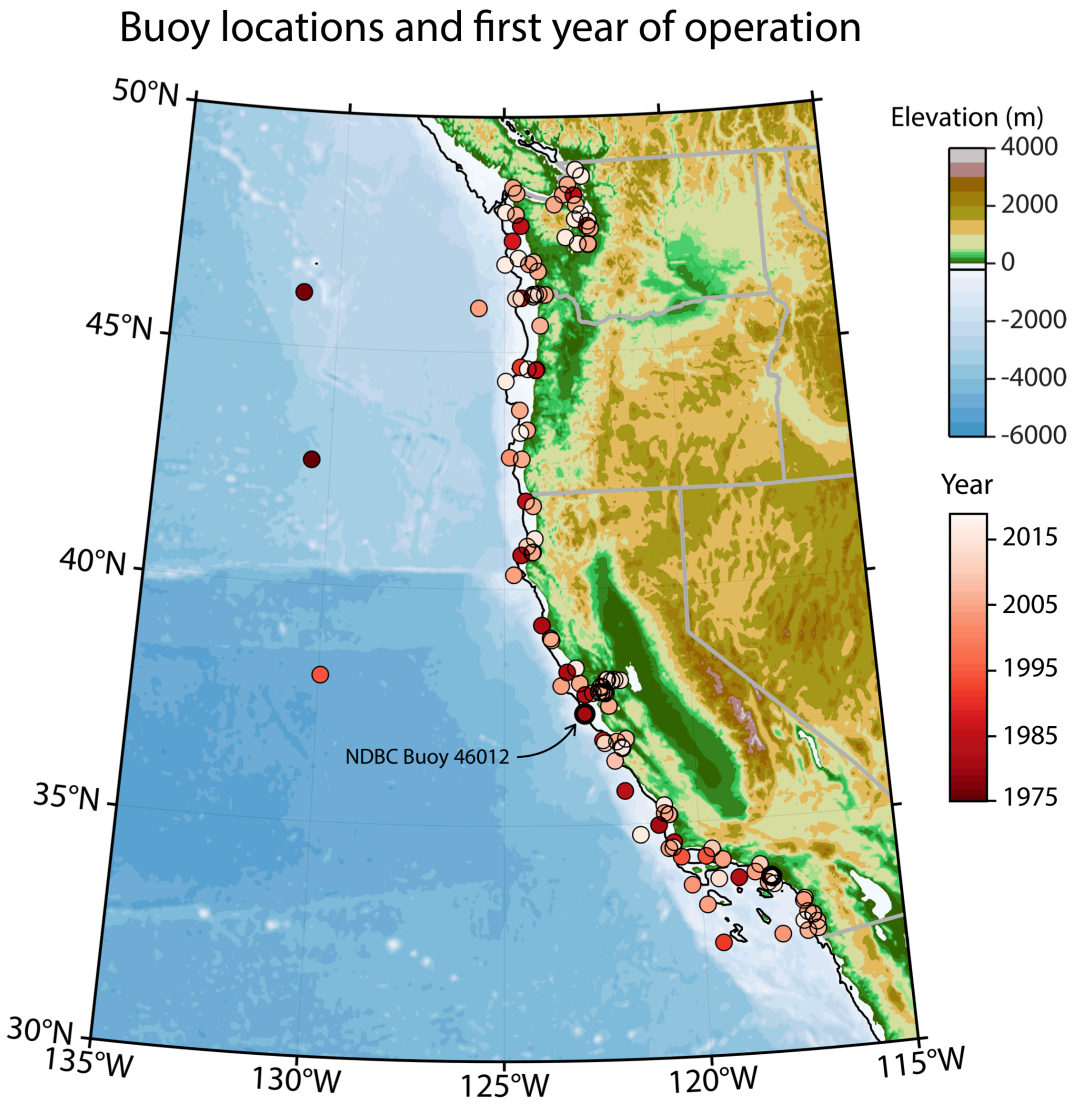

112 **Figure 1.** Locations of 138 buoys used in the analysis, color-coded by their first year of
113 measurements, are overlaid on topography and bathymetry. Most buoys are moored over the
114 continental shelf, typically within the 200m isobath (black curve). NDBC buoy 46012 (examined
115 in Figure 4) is indicated.
116

2. Data and Methods

2.1 Datasets and landfalling AR index

Our *in situ* dataset includes 138 over-shelf buoys throughout the U.S. west coast (32–49ºN) operated by NOAA's National Data Buoy Center (NDBC), Integrated Ocean Observing System partners, and the National Ocean Service. Generally, these buoys are moored over the continental shelf and constitute a spatially (alongshore) dense array of long-term (1975–present) measurements of critical boundary layer parameters, including air temperature, humidity (albeit only at a few buoys), surface pressure, and wind speed at the sub-hourly sampling rate. These measurements are averaged at hourly intervals to ensure consistency across the buoys. Figure 1 displays the location and starting year for all 138 buoys, superposed with topography and bathymetry based on ETOPO2 v2 (National Geophysical Data Center, 2006). No potentially biased spatial pattern is apparent in the starting years.

We use the COARE bulk flux algorithm v3.6 (Fairall et al., 2003) to compute LHF (Supplementary Materials S1.2). LHF is defined as positive upward (moisture/heat gain by ARs). Since most buoys do not record dewpoint temperature (T_d), we interpolate hourly near-surface T_d from ERA5 reanalysis on a $0.25° \times 0.25°$ grid (Hersbach et al., 2019) to buoy locations by distance-weighting each buoy's surrounding four reanalysis gridpoints. T_d from ERA5 is generally consistent with *in situ* T_d measurements available from 3 buoys (Figure S1).

To identify landfalling ARs, we use the SIO-R1, a catalog introduced by Gershunov et al. (2017) applying a new AR detection methodology to the NCEP/NCAR reanalysis (Kalnay et al. 1996). SIO-R1 reports at 6-hourly timesteps (1948–2017) whether regions satisfying AR conditions (≥15 mm total column water vapor (TCWV) and ≥250 kg/m/s vertically-integrated vapor transport (IVT), for ≥1500 km contiguous length) extend across any point along the North American west coast (20–60ºN). At every such timestep, it identifies the location of maximum IVT along the coast, providing IVT and TCWV there. SIO-R1 has been compared to other AR detection algorithms (Ralph et al., 2019b), showing a high level of consistency. We use SIO-R1 from 1979 to 2017 for the overlapping periods of the NDBC buoys and ERA5.

148 **2.2 AR compositing procedure**

149 We focus our analysis on strong (lifetime-maximum IVT ≥500 kg/m/s) and late-winter (January–
150 March) ARs. However, Figures S2–S5 show that variations of these criteria (lower vs. higher
151 intensity thresholds, and late vs. whole winters) yield very little changes in results. By selecting
152 stronger ARs (following the threshold of Shinoda et al., 2019), we intend to examine ARs with
153 robust air-sea interaction while ensuring that the analyzed ARs would be detected similarly by
154 alternate catalogs (Ralph et al., 2019b). We select JFM ARs to focus on events occurring when
155 ENSO's influence on coastal SST and west coast precipitation are most robust (Chelton and
156 Davis, 1982; Alexander et al., 2002; Frischknecht et al., 2015; Jong et al., 2016; Capotondi et al.,
157 2019).
158
159 SIO-R1 identifies 220 qualifying ARs that impact the U.S. coastline (32.5°–47.5°N) during their
160 lifetime. For each, we determine the lifetime southernmost and northernmost latitude of its
161 maximum IVT location given by SIO-R1. We include data from all buoys in that latitude range
162 (±1° on either side) for composites, averaging buoys within four equal latitudinal bins (4.25º
163 latitude). Composites are centered around each AR's 6-hourly timestep of lifetime maximum
164 IVT and extend 3 days before and after. While AR conditions as defined by a 250 kg/m/s IVT
165 threshold typically last 1–1.5 days at coastal locations, stronger ARs tend to last much longer
166 (Ralph et al., 2013; Rutz et al., 2014; Gershunov et al., 2017). Therefore, our longer compositing
167 window of ±3 days reflects the stringent intensity criteria. Since SIO-R1 provides IVT at only
168 one coastal location per timestep, we must define Day-0 on a coast-wide basis, despite the fact
169 that the maximum IVT might occur at different times along the coast. However, we find no
170 robust shift in the timing of AR conditions with latitude (Figure 2) even though ARs' landfalling
171 location tends to propagate southward along the coast (Figure S6).
172
173 For ENSO-phase composites, ARs are composited according to historical El Niño (La Niña)
174 years, defined as when the JFM-averaged Oceanic Niño Index (ONI) exceeds 0.5 (–0.5).
175 Different "flavors" of ENSO, as measured by, for example, the ENSO Longitude Index
176 (Williams and Patricola, 2018), are also known to affect ARs, but via different atmospheric
177 circulation responses (Kim et al., 2019). Furthermore, the mechanism by which non-canonical
178 ENSO modulates coastal SSTs is also likely different and event-dependent (e.g., Capotondi et

al., 2019). However, an extended analysis involving different types of ENSO is beyond the scope of the study.

3. Results

3.1 All-year and all-event composites

Figure 2 presents composite evolutions of near-surface meteorological quantities from buoys during all strong, late-winter landfalling ARs in 1979–2017, displaying surface pressure, wind speed, air temperature, SST, air-sea humidity gradient (all anomalies), and upward LHF (absolute). AR landfalls (Day-0) are associated with lower pressure, higher wind speed, and warmer and more humid air, and these anomalies extend to ±3 days of landfall. ARs' manifestation in the boundary layer meteorology tends to be most pronounced north of 40.5ºN (Oregon and Washington coasts), while AR frequency peaks around 40.5ºN (southern Oregon and northern California coasts). We find no coherent evolution of nearshore SST during ARs; thus, LHF evolution is mostly determined by atmospheric variability on synoptic timescales (Section 3.3). On interannual timescales, in contrast, SST variability becomes essential, as discussed in Section 3.2.

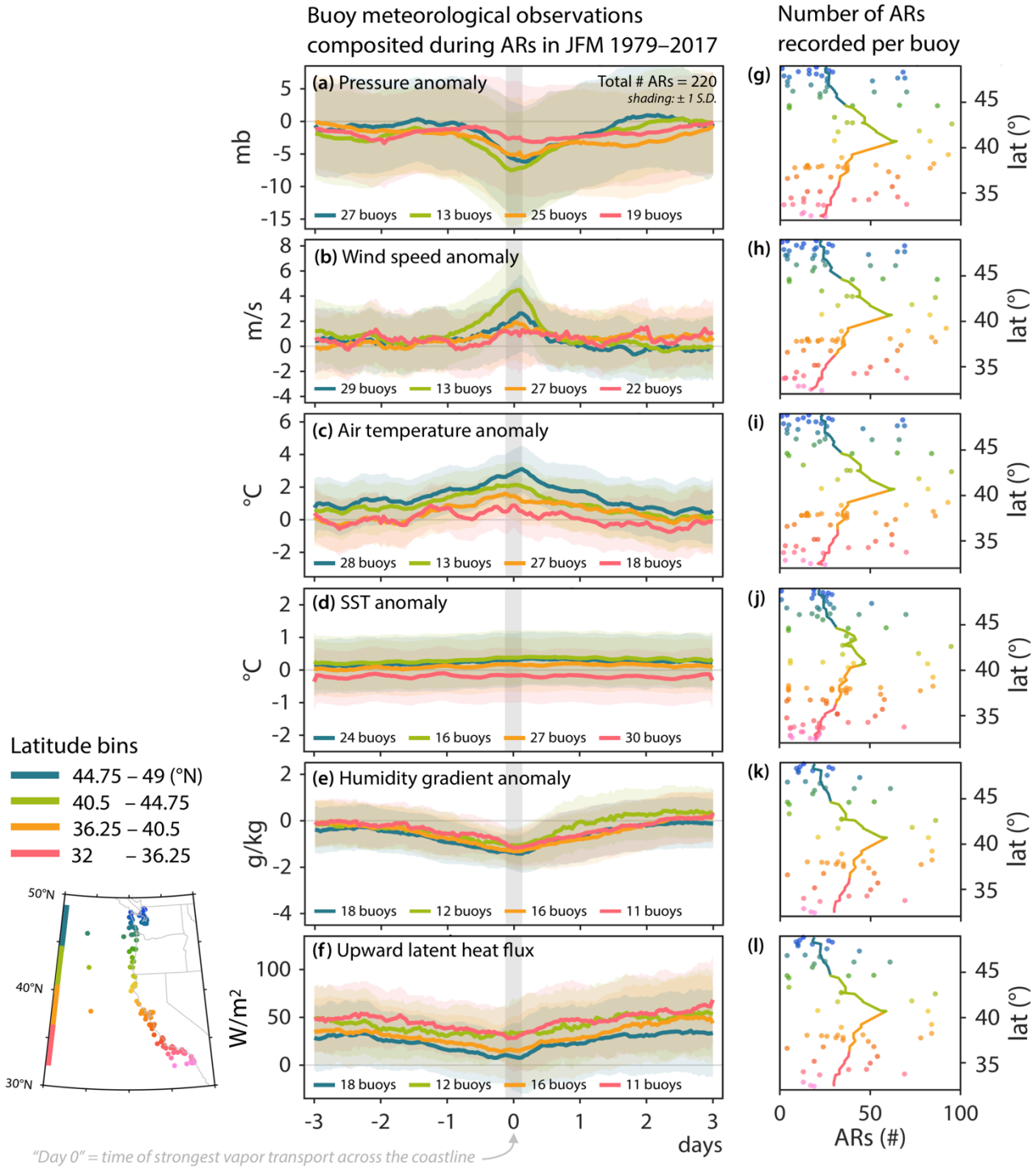

Figure 2. Composite evolution in (a) surface air pressure, (b) wind speed, (c) air temperature, (d) SST, and (e) humidity gradient (all anomalies), and (f) latent heat flux (absolute) during strong late-winter landfalling ARs (1979–2017). Gray vertical shading denotes the time of the ARs' maximum intensity. Colored curves and shading represent latitudinal bin averages and ±1 standard deviation, respectively. The number of buoys contributing to each bin average is indicated. (g–l)*:* the number of ARs recorded by each buoy (*x*-axis) for each quantity, plotted against buoy latitudes (*y*-axis). Line denotes 2° running averages.

Air-sea humidity gradient anomalies dominate the evolution of LHF during synoptic AR events. That is, despite strong winds associated with ARs, LHF typically weakens during peak intensity due to weakly negative humidity gradient anomalies (Shinoda et al., 2019). However, within Day ±1, when LHF is weakest (and LHF anomalies are negative; Figure S7), all latitudinal bin averages of absolute LHF remain positive. Absolute LHF typically ranges from 30–50 W/m^2 throughout total AR lifetimes (southern California, Oregon) or early and late lifetimes (northern California, Washington).

The shading, denoting standard deviation, in Figure 2 indicates substantial event-to-event variability. In particular, during extreme events, LHF may exhibit opposite evolution to the composite mean evolution (Figures 4, S4 & S8). For example, during a landfalling AR in February 2015 with intensity (lifetime-maximum coastal IVT) in the >95th percentile of all ARs in JFM 1979–2017, nearshore LHF was on average 30 W/m^2, with instantaneous estimates exceeding 60 W/m^2, along the central coast (36.25–40.5ºN) (Figure S8, Figure 4). This is in agreement with a similar time-mean LHF for the same AR reported by Shinoda et al. (2019) (their Figure 5b & S3) based on OAFLUX and CALWATER 2015 field measurements (Ralph et al., 2016). Our result adds that LHF estimated from nearshore buoys was similarly high on the southern coast (32–36.25ºN) and often exceeded 100 W/m^2 on the northern coast (40.5–45ºN) (Figure S8).

3.2 ENSO-phase composites

Figure 3a-c shows composite evolutions of LHF during landfalling ARs in El Niño and La Niña winters and their difference. LHF during the early and late stages of AR lifetimes (Day >±1) on the southern coast increases by >30 W/m^2, representing a ≥70% change, from La Niña to El Niño winters (Figure 3c). The northern coast sees an opposite change of similar magnitude, albeit with a weaker late-lifetime difference. This occurs during the portions of AR lifetimes when LHF is typically strongest (Figure 2). During ARs' peak intensity, within Day ±1, when LHF is smallest, the ENSO-related flux differences approach zero.

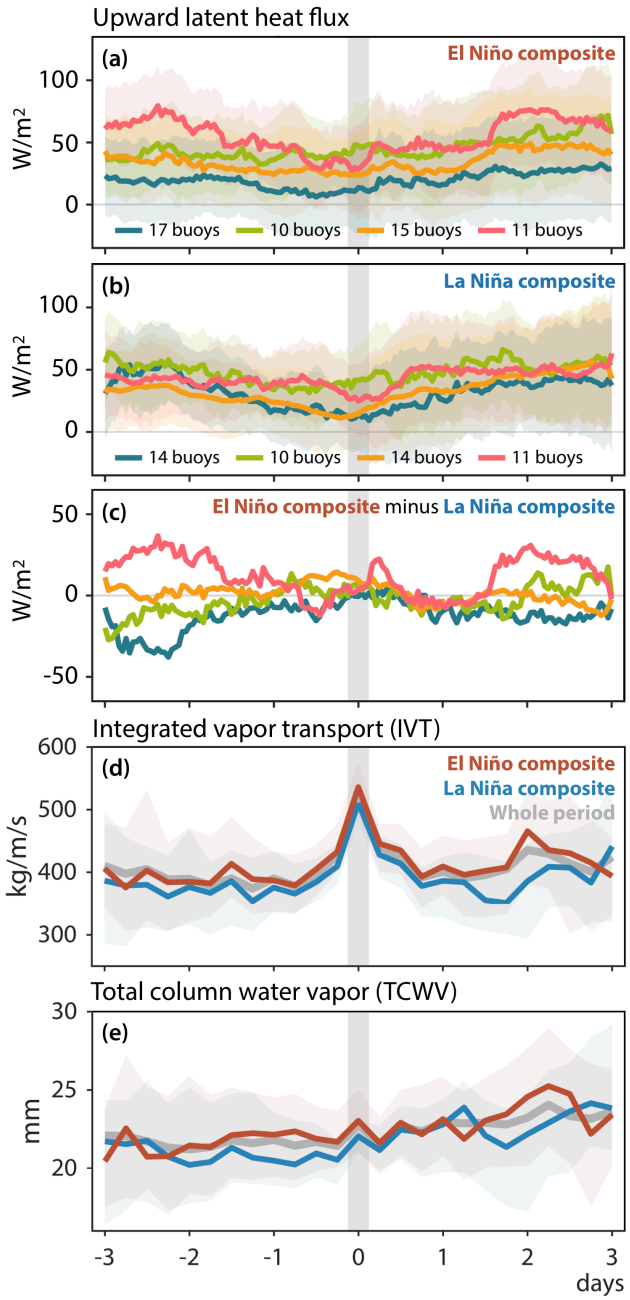

232 **Figure 3.** Composite evolutions of absolute latent heat flux during ARs in (a) El Niño and (b) La
233 Niña winters (1979–2017), and (c) El Niño minus La Niña for each latitudinal bin. (d–e):
234 Composite evolutions of two AR intensity metrics, IVT and TCWV, during ARs in El Niño
235 (red), La Niña (blue), and all (gray) winters (1950–2017).
236
237 Figure 3d-e shows ENSO-associated changes in AR intensity, as measured by IVT and TCWV
238 (from SIO-R1). Generally, AR intensity increases from La Niña to El Niño winters in both
239 metrics. Specifically, intensity increases most strongly before and after ARs' peak intensity (Day
240 >±1), with differences up to ~90 kg/m/s in IVT and ~2 mm in TCWV. The increases in AR

intensity >±1 day of landfall coincide with the periods when LHF is enhanced along the southern coast (Figures 3a,b). These AR intensity composites follow SIO-R1's AR intensity criteria (IVT ≥250 kg/m/s, relaxing our peak-IVT ≥500 kg/m/s criteria) and the period 1950–2017 common between SIO-R1 and ONI. The relaxed threshold and extended period chosen for this analysis maximize the sample sizes of ARs and ENSO years, and underscore the generality of these results (beyond only strong ARs and the temporal limitations imposed by the buoys and ERA5 data). However, our results remain unchanged even if we follow the more restrictive period and threshold (Figure S9).

3.3 Flux decomposition

We perform a linear decomposition of LHF to estimate contributions from constituent variables, following the procedure by Menezes et al. (2019; Supplementary Materials S1.2). Figure 4 presents a decomposition of LHF into estimated contributions from surface air stability (S = air temperature minus SST, positive stable), wind speed (U), relative humidity (RH), and SST.

To illustrate how to interpret this result, let us focus first on an extreme AR landfalling near San Francisco on February 5–7, 2015. The black-to-white dots in Figure 4a-d denote hourly results based on observations from NDBC buoy 46012, located off San Francisco, during this AR (Figure S8). The contributions to LHF (y-axis) were such that the strongest LHF (x-axis) was driven primarily by high wind speed, and partly by SST (note that SST's y-axis is 10x smaller). Meanwhile, stability and humidity mostly suppressed the LHF anomaly, or acted neutrally. While this was one extreme event, its demonstration of canonical AR features, such as strong wind and warm, moist air, lends confidence that the variables' LHF contributions seen here are consistent with ARs of average intensity.

Next, we extend the analysis to the whole late-winter (JFM) of the same year (2015), shown as color-coded scatters in Figure 4a–d. LHF anomalies were mostly near-zero or weakly negative. Nevertheless, the scattering indicates that strong positive LHF anomalies were primarily caused by high wind speed and dry air, and partly by SST anomalies. Negative LHF anomalies were mainly driven by low wind speed. SST anomalies contributed positively to LHF, likely because

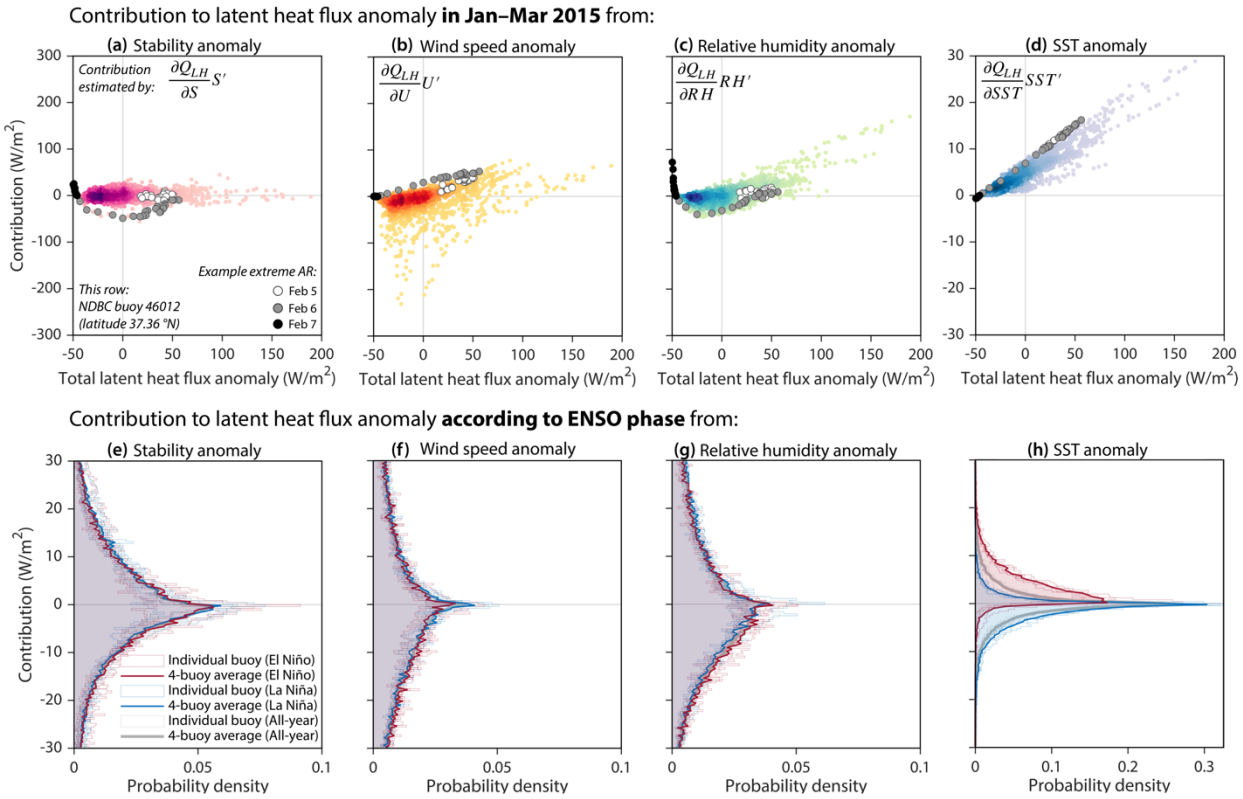

Figure 4. (a–d): *x*-axis: hourly upward latent heat flux (LHF) anomaly at NDBC buoy 46012 for January–March (JFM) 2015. *Y*-axis: contribution to that LHF anomaly from (a) air-sea stability, (b) wind speed, (c) relative humidity, and (d) SST anomalies. Color intensity indicates dot density. White-to-black dots denote 5-7 February during an extreme AR. Note the smaller *y*-scale for SST. (e–h): Distributions of LHF contributions are shown along the *y*-axis for El Niño JFM (red), La Niña JFM (blue), and all JFM (gray) in 1979–2017. Pale lines show individual histograms for four buoys along the coast; dark lines show average distributions across all four buoys. Note the larger *x*-scale for SST.

2015 was an El Niño year with anomalously warm SSTs. We also analyzed LHF contributions during only the few ARs affecting this buoy during JFM 2015, with complementary findings emphasizing the role of wind speed and partially SST strengthening LHF (Figure S10).

We also extend this decomposition analysis to all winters (JFM 1979–2017), first focusing only on Buoy 46012 (Figure S11), showing very similar results to the JFM2015 case (Figure 4a-d) except that SST's contributions are distributed both positively and negatively, as expected due to the inclusion of both El Niño and La Niña winters. In Figure 4e–h, for four buoys spanning the coast, we present probability distributions of contributions from each variable to LHF separately during El Niño winters, La Niña winters, and all winters. Whereas LHF contribution

distributions from stability, wind speed, and relative humidity are apparently independent of the ENSO phases, SST's contribution distribution clearly varies with the ENSO phases. Figures S12–S13 show the same results for each of the buoys separately.

4. Discussion

Our composite analyses of buoy-based LHF show that strong late-winter ARs landfalling along the U.S. west coast typically receive strong upward absolute LHF (30–50 W/m^2) 1–3 days before and after their landfalls. In contrast, during landfall (Day $\leq \pm 1$), LHF reaches its minimum (Figure 2). El Niño winters are associated with increased LHF along the southern coast and decreased LHF along the northern coast, while opposite changes occur during La Niña. Enhanced southern-coastal LHF during El Niño corresponds with generally intensified ARs (Figure 3). LHF decomposition revealed that during an El Niño winter at a buoy near San Francisco, strong LHF was primarily driven by high wind speed and dry air, while SST contributions were smaller but almost exclusively positive. These results raise several discussion points concerning the relationship between nearshore SST, LHF, and AR intensity.

First, the all-year and all-event composites show that nearshore LHF evolution during landfalling ARs primarily reflects the near-surface humidity gradient. However, although the evolutions of humidity gradient anomaly are almost identical between the different latitudinal bins, the evolutions of absolute LHF are not likely due to latitudinal variations in background SST. That is, the LHF is strongest along the southern coast, where SST is warmer, even though the air is also warmer and moister. Latitudinal variations in background SST are therefore a primary factor influencing the LHF experienced by landfalling ARs on synoptic time-scales.

How, then, may temporal variations in background SST, mainly driven by ENSO on interannual timescales, contribute to LHF variations during ARs? We found that along the entire coast, and not necessarily limited to AR conditions, SST anomalies strengthen LHF during El Niño winters and weaken it during La Niña. In contrast, the effects of relative humidity, wind speed, and near-surface stability on LHF remain mostly unchanged between ENSO phases (Figure 4, S12, S13). Therefore, we propose that, while other variables drive nearshore LHF variations on synoptic timescales, ENSO-induced SST variations are the primary contributor to interannual variations in

AR-associated LHF. However, SST anomalies' effect on LHF may be limited along the northern coast, where LHF tends to be weaker during El Niño ARs despite warm SST anomalies (Figures 3c and 4h).

Finally, Figure 3 suggests a potential relationship between nearshore LHF and AR intensity. ARs typically intensify during El Niño winters along the southern coast. The midlatitude storm track shifts southward during El Niño (Trenberth et al., 1998; Seager et al., 2010), with average ARs landfalling latitude also shifting southward (Figure S6, Payne and Magnusdottir, 2014). Since we find that nearshore LHF increases during El Niño along the southern coast, the intensified ARs in El Niño winters would experience both climatologically stronger (due to latitude) and anomalously enhanced (due to ENSO) LHF during landfall. Recent studies emphasize that large-scale circulation changes over the Pacific enhance onshore IVT during El Niño, intensifying southwestern U.S. precipitation (Kim and Alexander, 2015; Guirguis et al., 2018; Kim et al., 2019). Our results suggest that the local contribution from enhanced nearshore LHF may also play a role in intensifying ARs during El Niño (Chen and Leung, 2020).

Persson et al. (2005) observed that nearshore turbulent heat fluxes in southern California significantly destabilized boundary layer air in a landfalling AR. From offshore LHF of 32 W/m^2 derived from field measurements, they estimated boundary-layer convective available potential energy (CAPE) to be enhanced by 26% as the AR approached the shore, proposing that nearshore SST anomalies during El Niño had likely enabled this effect. Our results support this by demonstrating covariability between nearshore SST, LHF, and landfalling AR intensity during El Niño. Furthermore, while Persson et al. (2005)'s study was limited to a single AR during an El Niño year at southern latitude, we observe that absolute LHF typically exceeds 30 W/m^2 throughout all or some of AR lifetimes at all coastal latitudes (Figure 3a-c), implying that the conditions for such an effect of coastal LHF on ARs may occur more generally, extending to northern latitudes and non-El Niño years.

5. Conclusions

This study characterizes nearshore air-sea interaction during landfalling ARs by making use of 138 over-shelf buoys to observe coastal meteorology and SST along the U.S. west coast.

Collectively, these moored observations enable a systematic synoptic-scale analysis of a multi-decadal (39-year) record of ARs through their high spatial (alongshore) density and fine temporal resolution. Because the buoys are mostly moored over the continental shelf, with typical coastal proximities under 30 km, they can offer a unique view of coastal air-sea processes at the time of AR landfall.

Late-winter ARs experience upward LHF throughout their 6-day landfalling lifetimes, despite LHF weakening within ±1 day of events' peak intensity. LHF typically exceeds 30 W/m^2 throughout partial or total AR lifetimes and is strongest at southernmost and weakest at northernmost latitudes. As indicated in a case study by Persson et al. (2005), nearshore LHF of such magnitudes may be sufficient to destabilize the nearshore boundary layer air, potentially intensifying subsequent precipitation. With our extended period and region examined, we demonstrate that such interaction between ARs and the coastal ocean through LHF may be more ubiquitous.

During El Niño winters along the southern coast, nearshore LHF increases by ~30 W/m^2 (>70%) from La Niña winters, during ±1–3 days from ARs' peak intensity. Opposite changes occur along the northern coast. The enhanced LHF along the southern coast early and late in AR landfalling lifetimes coincides with intensified ARs during El Niño. AR intensification is most strongly manifested early and late in their landfalling lifetimes, though it is ostensible throughout (Figure 3d-e).

Finally, flux decomposition demonstrates that LHF is primarily controlled by wind speed, relative humidity, and stability on synoptic to seasonal timescales. However, on interannual timescales, SST anomalies modulated by ENSO dominantly control the variations in LHF experienced by ARs between different ENSO phases.

Acknowledgments

This project is part of STB's Summer Student Fellowship (SSF) program at Woods Hole Oceanographic Institution (WHOI) sponsored by the National Science Foundation (NSF) Research Experience for Undergraduates Program (NSF REU OCE-1852460). HS acknowledges

the support from NSF OCE-2022846, CCU from the NSF PREEVENTS program (OCE-1663704), and JDS from NOAA under NA17OAR4310255, and Buoy data available at https://bit.ly/3g4LByx, SIO-R1 at https://bit.ly/2CS15aE, and ERA5 at https://bit.ly/2X3HivE. The authors thank the anonymous reviewers for their constructive comments, which helped to improve the manuscript substantially.

References

Alexander, M. A., Bladé, I., Newman, M., Lanzante, J. R., Lau, N.-C., & Scott, J. D. (2002). The Atmospheric Bridge: The Influence of ENSO Teleconnections on Air–Sea Interaction over the Global Oceans. *Journal of Climate,* 15(16), 2205–2231.

Capotondi, A., Sardeshmukh, P. D., Di Lorenzo, E., Subramanian, A. C., & Miller, A. J. (2019). Predictability of US West Coast Ocean Temperatures is not solely due to ENSO. *Scientific Reports*, 9(1), 10993.

Corringham, T. W., Ralph, F. M., Gershunov, A. Cayan, D. R., & Talbot, C. A. (2019). Atmospheric Rivers Drive Flood Damages in the Western United States. *Sci. Adv*., 5, 1–7.

Chelton, D. B., & Davis, RÍ. E. (1982). Monthly Mean Sea-Level Variability Along the West Coast of North America. *Journal of Physical Oceanography,* 12(8), 757–784.

Chen, X., & Leung, L. R. (2020). Response of Landfalling Atmospheric Rivers on the U.S. West Coast to Local Sea Surface Temperature Perturbations. *Geophysical Research Letters*, 47(18), e2020GL089254.

Dettinger, M. D. (2013). Atmospheric Rivers as Drought Busters on the U.S. West Coast. *Journal of Hydrometeorology*, 14(6), 1721–1732.

Dettinger, M., and Coauthors 2012: Design and quantification of an extreme winter storm scenario for emergency preparedness and planning exercises in California*. Nat. Hazards*, 60, 1085–1111.

Dettinger, M. D., Ralph, F. M., Das, T., Neiman, P. J., & Cayan, D. R. (2011). Atmospheric Rivers, Floods and the Water Resources of California. *Water*, 3(2), 445–478.

Fairall, C. W., Bradley, E. F., Hare, J. E., Grachev, A. A., & Edson, J. B. (2003). Bulk Parameterization of Air–Sea Fluxes: Updates and Verification for the COARE Algorithm. *Journal of Climate*, 16(4), 571–591.

415 Frischknecht, M., Münnich, M., & Gruber, N. (2015). Remote versus local influence of ENSO
416 on the California Current System. *Journal of Geophysical Research: Oceans,* 120(2),
417 1353–1374.
418 Gershunov, A., Shulgina, T., Ralph, F. M., Lavers, D. A., & Rutz, J. J. (2017). Assessing the
419 climate-scale variability of atmospheric rivers affecting western North America.
420 *Geophysical Research Letters*, 44, 7900–7908.
421 Gonzales, K. R., Swain, D. L., Nardi, K. M., Barnes, E. A., & Diffenbaugh, N. S. (2019). Recent
422 Warming of Landfalling Atmospheric Rivers Along the West Coast of the United States.
423 *Journal of Geophysical Research: Atmospheres*, 124(13), 6810–6826.
424 Guan, B., Molotch, N. P., Waliser, D. E., Fetzer, E. J., & Neiman, P. J. (2010). Extreme snowfall
425 events linked to atmospheric rivers and surface air temperature via satellite
426 measurements. *Geophysical Research Letters,* 37(20), L20401.
427 Guirguis, K., Gershunov, A., Clemesha, R. E. S., Shulgina, T., Subramanian, A. C., & Ralph, F.
428 M. (2018). Circulation Drivers of Atmospheric Rivers at the North American West Coast.
429 *Geophysical Research Letters*, 45(22), 12,576-12,584.
430 Hersbach, H., Bell, B., Berrisford, P., Hirahara, S., Horányi, A., Muñoz-Sabater, J., Nicolas, J.,
431 Peubey, C., Radu, R., Schepers, D., Simmons, A., Soci, C., Abdalla, S., Abellan, X.,
432 Balsamo, G., Bechtold, P., Biavati, G., Bidlot, J., Bonavita, M., … Thépaut, J.-N. (2020).
433 The ERA5 global reanalysis. Quarterly Journal of the Royal Meteorological Society,
434 146(730), 1999–2049. https://doi.org/10.1002/qj.3803
435 Jong, B.-T., Ting, M., & Seager, R. (2016). El Niño's impact on California precipitation:
436 seasonality, regionality, and El Niño intensity. *Environmental Research Letters*, 11(5),
437 054021.
438 Kalnay, E., and Co-authors (1996), The NCEP/NCAR 40-Year Reanalysis Project. *Bull. Amer.*
439 *Met. Soc*., 77, 437-471.
440 Kim, H.-M., & Alexander, M. A. (2015). ENSO's Modulation of Water Vapor Transport over
441 the Pacific–North American Region. *Journal of Climate*, 28(9), 3846–3856.
442 Kim, H.-M., Zhou, Y., & Alexander, M. A. (2019). Changes in atmospheric rivers and moisture
443 transport over the Northeast Pacific and western North America in response to ENSO
444 diversity. *Climate Dynamics*, 52(12), 7375–7388.

445 Lavers, D. A., Allan, R. P., Wood, E. F., Villarini, G., Brayshaw, D. J. & Wade, A. J (2011). Winter
446 floods in Britain are connected to atmospheric rivers. *Geophys. Res. Lett*., 38, L23803,
447 doi:10.1029/2011GL049783.
448 Leung, L. R., & Qian, Y. (2009). Atmospheric rivers induced heavy precipitation and flooding in
449 the western U.S. simulated by the WRF regional climate model. *Geophys. Res. Lett*., 36,
450 L03820, doi:10.1029/2008GL036445.
451 Menezes, V. V., Farrar, J. T., & Bower, A. S. (2019). Evaporative Implications of Dry-Air
452 Outbreaks Over the Northern Red Sea. *Journal of Geophysical Research: Atmospheres*,
453 124(9), 4829–4861.
454 Meyers, S. D., Melsom, A., Mitchum, G. T., & O'Brien, J. J. (1998). Detection of the fast Kelvin
455 wave teleconnection due to El Niño-Southern Oscillation. *Journal of Geophysical*
456 *Research: Oceans,* 103(C12), 27655–27663
457 Moore, B. J., Neiman, P. J., Ralph, F. M., & Barthold, F. E. (2012). Physical Processes
458 Associated with Heavy Flooding Rainfall in Nashville, Tennessee, and Vicinity during 1–
459 2 May 2010: The Role of an Atmospheric River and Mesoscale Convective
460 Systems. *Mon. Wea. Rev.*, 140, 358–378,
461 Neiman, P. J. , Ralph, F. M., Wick, G. A., Kuo, Y.-H., Wee, T.-K., Ma, Z,. Taylor, G. H,. and
462 Dettinger, M. D. (2008a). Diagnosis of an intense atmospheric river impacting the Pacific
463 Northwest: Storm summary and offshore vertical structure observed with COSMIC
464 satellite retrievals. Mon. Wea. Rev., 136, 4398–4420.
465 Neiman, P. J., Schick, L. J., Ralph, F. M., Hughes, M., & Wick, G. A. (2011). Flooding in
466 Western Washington: The Connection to Atmospheric Rivers. *Journal of*
467 *Hydrometeorology*, 12(6), 1337–1358.
468 Payne, A. E., & Magnusdottir, G. (2014). Dynamics of Landfalling Atmospheric Rivers over the
469 North Pacific in 30 Years of MERRA Reanalysis. *Journal of Climate*, 27(18), 7133–
470 7150.
471 Persson, P. O. G., Neiman, P. J., Walter, B., Bao, J.-W., & Ralph, F. M. (2005). Contributions
472 from California Coastal-Zone Surface Fluxes to Heavy Coastal Precipitation: A CALJET
473 Case Study during the Strong El Niño of 1998. *Monthly Weather Review*, 133(5), 1175–
474 1198.

Ralph, F. M., Wilson, A. M., Shulgina, T., Kawzenuk, B., Sellars, S., Rutz, J. J., Lamjiri, M. A., Barnes, E. A., Gershunov, A., Guan, B., Nardi, K. M., Osborne, T., & Wick, G. A. (2019b). ARTMIP-early start comparison of atmospheric river detection tools: How many atmospheric rivers hit northern California's Russian River watershed? *Climate Dynamics*, 52(7), 4973–4994.

Ralph, F. M., Rutz, J. J., Cordeira, J. M., Dettinger, M., Anderson, M., Reynolds, D., Schick, L. J., & Smallcomb, C. (2019a). A Scale to Characterize the Strength and Impacts of Atmospheric Rivers. Bull. Amer. Meteor. Soc., 100, 269-289.

Ralph, F. M., Prather, K. A., Cayan, D., Spackman, J. R., DeMott, P., Dettinger, M., Fairall, C., Leung, R., Rosenfeld, D., Rutledge, S., Waliser, D., White, A. B., Cordeira, J., Martin, A., Helly, J., & Intrieri, J. (2016). CalWater Field Studies Designed to Quantify the Roles of Atmospheric Rivers and Aerosols in Modulating U.S. West Coast Precipitation in a Changing Climate. *Bulletin of the American Meteorological Society,* 97(7), 1209–1228.

Ralph, F. M., Coleman, T., Neiman, P. J., Zamora, R. J., & Dettinger, M. D. (2013). Observed Impacts of Duration and Seasonality of Atmospheric-River Landfalls on Soil Moisture and Runoff in Coastal Northern California. *Journal of Hydrometeorology*, 14(2), 443–459.

Ralph, F. M., & Dettinger, M. D. (2012). Historical and national perspectives on extreme West Coast precipitation associated with atmospheric rivers during December 2010. *Bull. Amer. Meteor. Soc.*, **93**, 783–790.

Ralph, F. M., Neiman, P. J., Kiladis, G. N., Weickman, K., & Reynolds, D. W. (2011). A multi-scale observational case study of a Pacific atmospheric river exhibiting tropical–extratropical connections and a mesoscale frontal wave. Mon. Wea. Rev., 139, 1169–1189.

Ralph, F. Martin, Neiman, P. J., Wick, G. A., Gutman, S. I., Dettinger, M. D., Cayan, D. R., & White, A. B. (2006). Flooding on California's Russian River: Role of atmospheric rivers. *Geophy. Res. Lett.*. 33, L13801.

Ralph, F. Martin, Neiman, P. J., & Rotunno, R. (2005). Dropsonde Observations in Low-Level Jets over the Northeastern Pacific Ocean from CALJET-1998 and PACJET-2001: Mean Vertical-Profile and Atmospheric-River Characteristics. *Monthly Weather Review*, 133(4), 889–910.

Ralph, F. M., Neiman, P. J., & Wick, G. A. (2004). Satellite and CALJET Aircraft Observations of Atmospheric Rivers over the Eastern North Pacific Ocean during the Winter of 1997/98. *Monthly Weather Review,* 132(7), 1721–1745.

Rutz, J. J., Steenburgh, W. J., & Ralph, F. M. (2014). Climatological Characteristics of Atmospheric Rivers and Their Inland Penetration over the Western United States. *Monthly Weather Review*, 142(2), 905–921.

Schwing, F. B., Murphree, T., deWitt, L., & Green, P. M. (2002). The evolution of oceanic and atmospheric anomalies in the northeast Pacific during the El Niño and La Niña events of 1995 2001. *Progress in Oceanography,* 54*,* 459–491.

Seager, R., Kushnir, Y., Nakamura, J., Ting, M., & Naik, N. (2010). Northern Hemisphere winter snow anomalies: ENSO, NAO and the winter of 2009/10. *Geophysical Research Letters*, 37(14), L14703.

Shinoda, T., Zamudio, L., Guo, Y., Metzger, E. J., & Fairall, C. W. (2019). Ocean variability and air-sea fluxes produced by atmospheric rivers. *Scientific Reports, 9*(1), 2152.

Simpson, J. J. (1984). El Nino-induced onshore transport in the California Current during 1982-1983. *Geophysical Research Letters,* 11(3), 233–236.

Smith, B. L., S. E. Yuter, P. J. Neiman, and D. E. Kingsmill, 2010: Water vapor fluxes and orographic precipitation over northern California associated with a land-falling atmospheric river. Mon. Wea. Rev., 138, 74–100.

Todd, R. E., Rudnick, D. L., Davis, R. E., & Ohman, M. D. (2011). Underwater gliders reveal rapid arrival of El Niño effects off California's coast. *Geophysical Research Letters,* 38(3), L03609.

Trenberth, K. E., Branstator, G. W., Karoly, D., Kumar, A., Lau, N.-C., & Ropelewski, C. (1998). Progress during TOGA in understanding and modeling global teleconnections associated with tropical sea surface temperatures. *Journal of Geophysical Research: Oceans*, 103, 14291–14324.

White, A. B., & Coauthors (2012) NOAA's rapid response to the Howard A. Hanson Dam flood risk management crisis. *Bull. Amer. Meteor. Soc.*, **93**, 189–207.

Williams, I. N., & Patricola, C. M. (2018). Diversity of ENSO Events Unified by Convective Threshold Sea Surface Temperature: A Nonlinear ENSO Index. *Geophysical Research Letters*, 45(17), 9236–9244.

Yu, L., & Weller, R. A. (2007). Objectively Analyzed Air–Sea Heat Fluxes for the Global Ice-Free Oceans (1981–2005). *Bulletin of the American Meteorological Society*, 88(4), 527–540.

Zhang, Z., Ralph, F. M., & Zheng, M. (2019). The relationship between extratropical cyclone strength and atmospheric river intensity and position. *Geophysical Research Letters*, 46, 1814– 1823.

Zhu, Y., & Newell, R. E. (1998). A Proposed Algorithm for Moisture Fluxes from Atmospheric Rivers. *Monthly Weather Review*, 126(3), 725–735.

References from the Supporting Information

Bosilovich, M. G., Robertson, F. R., Takacs, L., Molod, A., & Mocko, D. (2017). Atmospheric Water Balance and Variability in the MERRA-2 Reanalysis. *Journal of Climate, 30*(4), 1177–1196.

Emanuel, K. A. (1994). *Atmospheric Convection*. Oxford University Press.

Richter, I., & Xie, S.-P. (2008). Muted precipitation increase in global warming simulations: A surface evaporation perspective. *Journal of Geophysical Research: Atmospheres*, 113, D24118.

Vimont, D. J., Alexander, M., & Fontaine, A. (2009). Midlatitude Excitation of Tropical Variability in the Pacific: The Role of Thermodynamic Coupling and Seasonality. *Journal of Climate,* 22(3), 518–534.

Geophysical Research Letters

Supporting Information for

The role of nearshore air-sea interactions for landfalling atmospheric rivers on the U.S. West Coast

Samuel Bartusek[1,2], Hyodae Seo[2], Caroline C. Ummenhofer[2], John Steffen[2]

[1]Department of Geosciences, Princeton University, [2]Department of Physical Oceanography, Woods Hole Oceanographic Institution

Contents of this file

S1. Latent heat flux calculation and decomposition procedures

S1.1 Latent heat flux calculation

To calculate latent heat flux (LHF), we use the COARE algorithm, version 3.6 (Fairall et al., 2003), based on the standard air-sea bulk flux formula

$$Q_{LH} = \rho L_e c_e U\left(q_s - q_a\right), \ldots (1)$$

where U is wind speed, q_s is surface specific humidity (a function of SST), q_a is near-surface air humidity (thus, $q_s - q_a$ being the surface to near-surface vertical humidity gradient), ρ is the density of air, L_e is the latent heat of evaporation, and c_e is the turbulent exchange coefficient.

S1.2 Linear flux decomposition procedure

Our flux decomposition procedure follows Menezes et al. (2019), an approach similar to Bosilovich et al. (2017), Richter and Xie (2008), and Vimont et al. (2009). We first rewrite the bulk formula for LHF in terms of the variables we are interested in disentangling, i.e., U, SST, relative humidity (RH), and near-surface air stability ($S = T_a - SST$):

$$Q_{LH} = \rho L_e c_e U\left[q_s(SST) - RH \cdot q_a(SST + S)\right] \ldots (2)$$

By linearizing this equation about a mean state and using a first-order Taylor expansion, the anomalous LHF at a given time can be approximated as the sum of contributions caused by anomalies in each variable,

$$Q_{LH}{}' = \frac{\partial Q_{LH}}{\partial U}U' + \frac{\partial Q_{LH}}{\partial RH}RH' + \frac{\partial Q_{LH}}{\partial S}S' + \frac{\partial Q_{LH}}{\partial SST}SST' + \frac{\partial Q_{LH}}{\partial c_e}c_e{}' + \frac{\partial Q_{LH}}{\partial \rho}\rho', \ldots (3)$$

where primes indicate departures from a mean state. We calculate anomalies from the whole-record spline-interpolated monthly climatology at each buoy location, and treat space- and time-interpolated ERA5 dewpoint temperature as a substitute buoy variable. Partial derivatives in Eq. 3 can be given analytically by

$$\frac{\partial Q_{LH}}{\partial U} = \frac{Q_{LH}}{U}, \ldots(4)$$

$$\frac{\partial Q_{LH}}{\partial RH} = -\frac{Q_{LH}}{\alpha - RH}, \ldots(5)$$

$$\frac{\partial Q_{LH}}{\partial S} = -Q_{LH}\frac{RH\left[(b/(SST+S)^2 - c/(SST+S)\right]}{\alpha - RH}, \ldots(6)$$

$$\frac{\partial Q_{LH}}{\partial SST} = Q_{LH}\frac{\alpha(b/SST^2 - c/SST) - RH\left[b/(SST+S)^2 - c/(SST+S)\right]}{\alpha - RH}, \ldots(7)$$

with

$$\alpha \equiv exp\left\{\frac{b}{SST+S} - \frac{b}{SST} - cln\left(\frac{S}{SST+S}\right)\right\} \ldots(8)$$

and constants $b = 6{,}743\,.769$, and $c = 4.8451$, from Emanuel (1994).

S2. Single-AR case study

Our assessment of AR-associated LHFs includes a case study analyzing one particular AR event that made landfall along much of the U.S. west coast from February 1–9, 2015 (according to SIO-R1; Gershunov et al., 2017). Figure S2 shows the latitudinal bin averages of absolute upward LHF, as in Figure 2. Shown above the LHF data, corresponding to the right y-axis and the map to the right, is the latitude of maximum IVT along the coastline at every 6-hourly AR index timestep (i.e., its "landfalling location"). Since this particular AR reached its maximum intensity (IVT) at 0600 UTC February 6th, we center this analysis around that timestep, extending three days before and after constructing the time series. Although the AR-associated extratropical cyclone propagates eastward, the AR's region of influence along the coastline travels roughly southward, from the Oregon coast on February 4th toward southern California by February 9th, due in part to the coastline's shape.

During this strong AR, we see an *enhanced* absolute upward LHF that peaks near the AR's time and location of peak intensity, which is in contrast to the all-year composite results. In particular, the bin average over 40.5–44.75ºN (green) reaches 100 W/m^2 within one day before the event peak, with the positive one standard deviation envelope exceeding 150 W/m^2. The southward movement of the AR center is also indicated by the enhanced upward LHF subsequently found to the southern latitudes (orange and pink), whose peaks also reach up to 50 W/m^2. Within a day following the AR's maximum intensity, upward LHF in all bin averages reduces to near-zero, and some bin averages become negative (indicating the atmosphere is losing heat to the ocean).

S3. Supplementary Figures

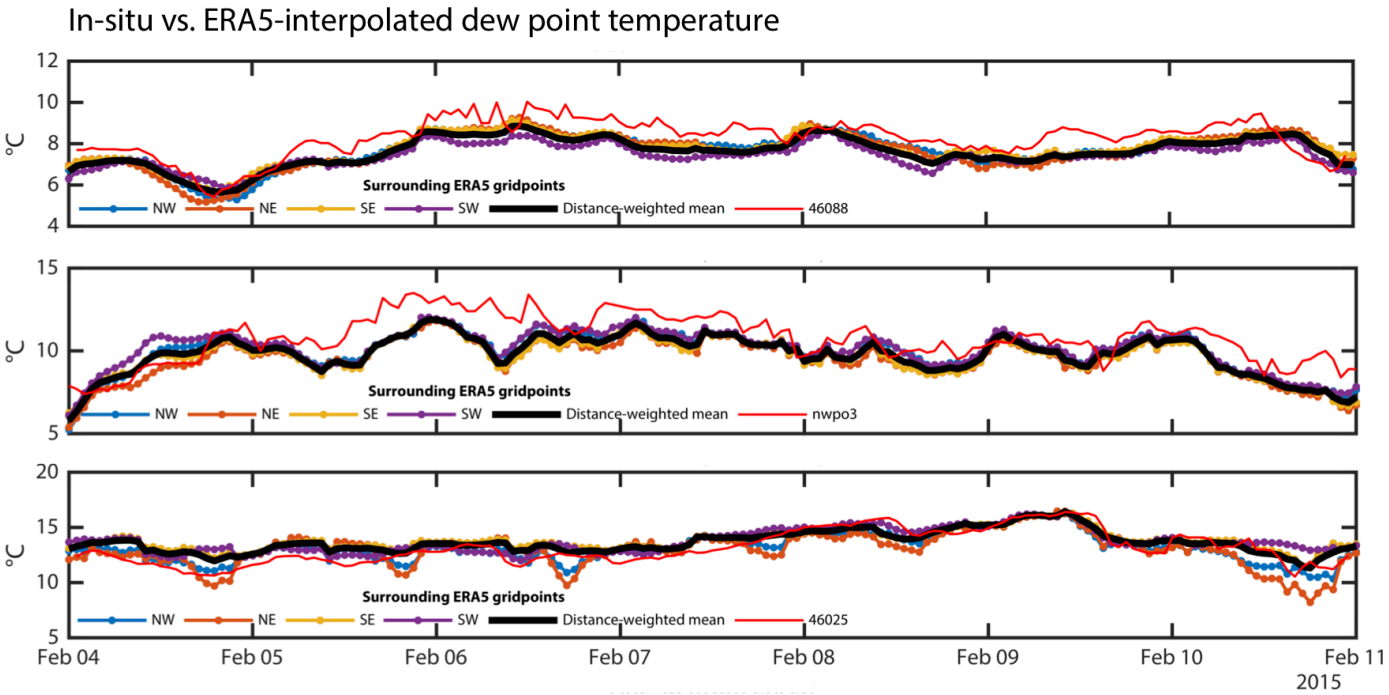

Figure S1. Comparison of in-situ vs. ERA5 dewpoint temperature during the case-study AR event in February 2015. During this period, dewpoint temperature measurements are available from the three buoys (46088, nwpo3, and 46025, thin red lines). The ERA5 dewpoint temperature data are also shown at each buoy's four surrounding gridpoints (colored dotted lines) and distance-weighted averages (thick black lines).

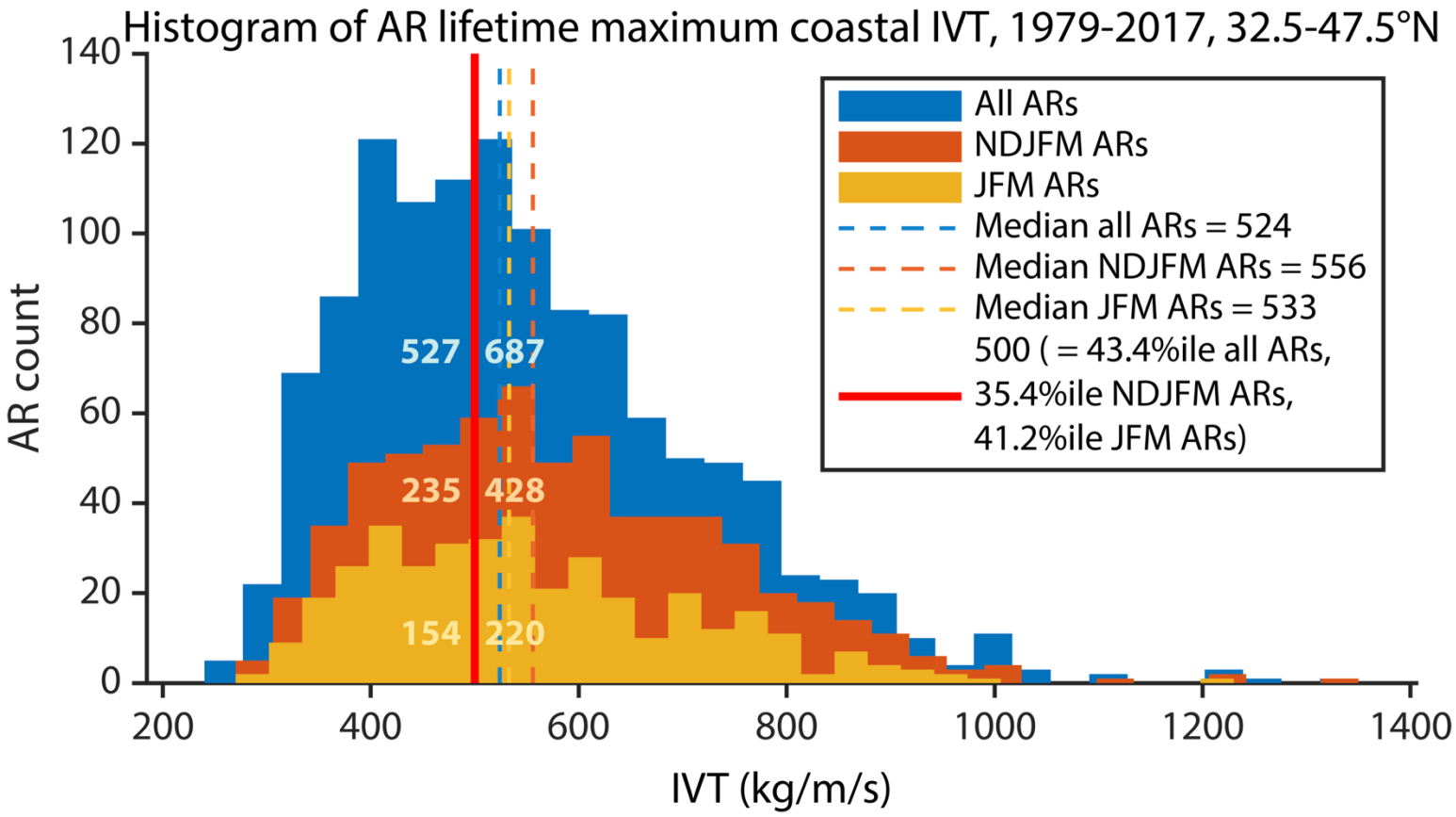

Figure S2. Histograms of lifetime-maximum coastal IVT for ARs impacting the U.S. coast in 1979–2017. Maximum IVT for ARs in all months, November–March, and January–March are shown as the blue, orange, and yellow histograms, respectively, with the *y*-axis showing the raw AR count. Dashed lines show the median for each histogram, with the exact values indicated in the legend. The red vertical line shows 500 kg/m/s IVT, which corresponds with the AR intensity threshold used in our main analysis. The legend reports what percentile of AR intensities 500 kg/m/s corresponds to within each month range. Pale bold numbers on the histograms on either side of the red line indicate the number of ARs below and above the 500 kg/m/s lifetime-maximum coastal IVT threshold, for each month range considered.

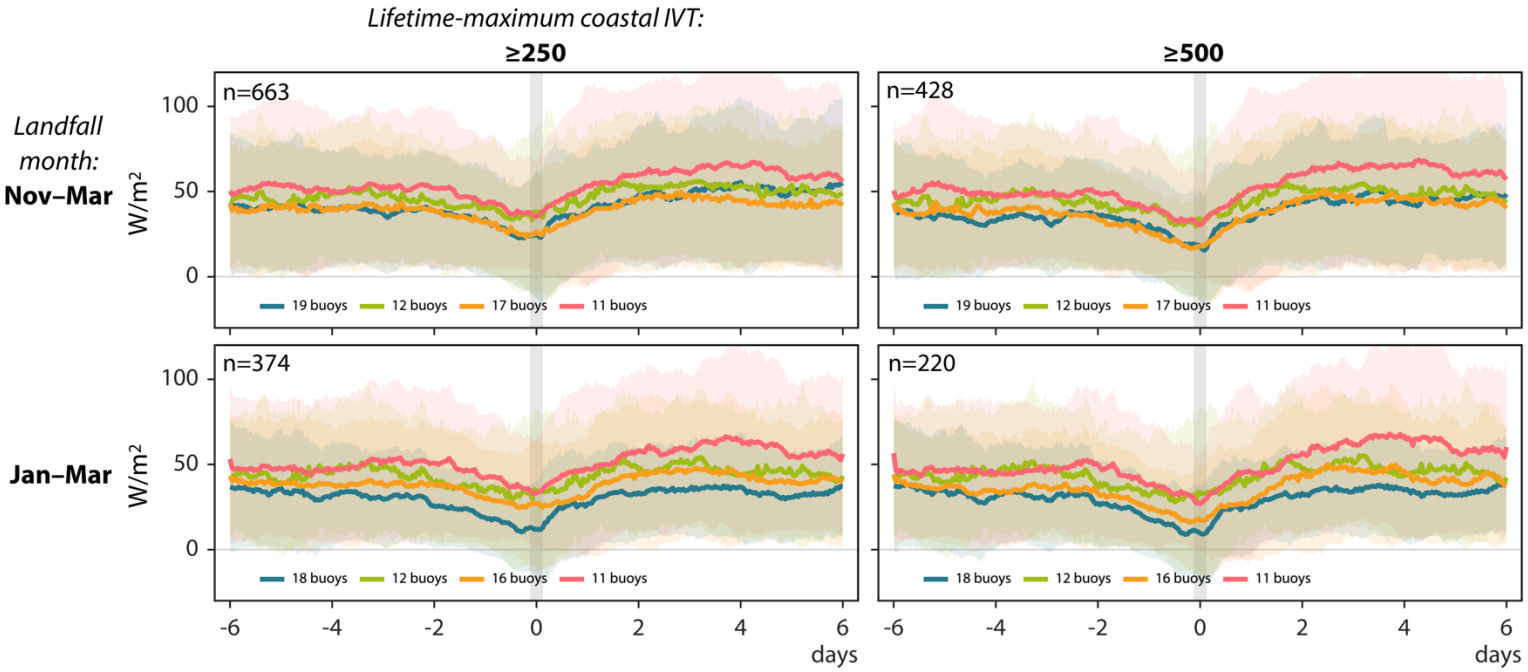

Figure S3. Absolute coastal latent heat flux composites for winter-landfalling ARs in 1979–2017, according to differing seasonal definitions and intensity thresholds. Seasonal definition is varied across rows (composites considering ARs landfalling in November–March, or "extended winter", vs. in January–March), and intensity threshold is varied across columns (composites considering ARs with lifetime-maximum coastal IVT at least 250 vs. 500 kg/m/s). Thus, the bottom right plot is the same composite as shown in the main analysis, considering only ARs landfalling in January–March, and only with at least 500 kg/m/s lifetime-maximum IVT (Figure 2f). Bin averages are as shown in the main analysis. Composites extend ±6 days from Day 0, as opposed to ±3 days as shown in the main analysis, to provide a longer context. The number of ARs considered for each composite are indicated (i.e., corresponding with the numbers in Figure S2).

Latent heat flux during ARs in JFM 1979–2017, composited by lifetime-maximum IVT percentile range

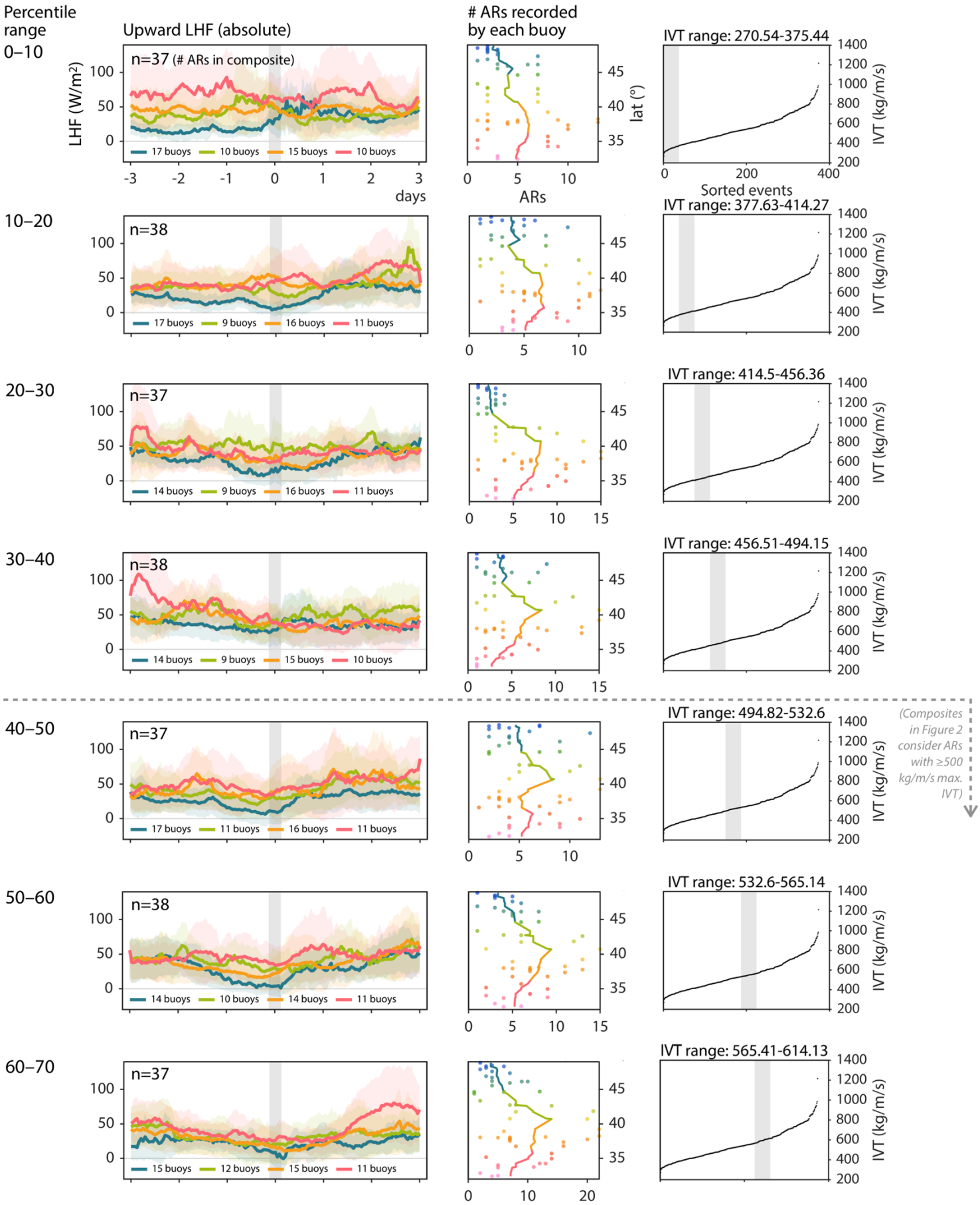

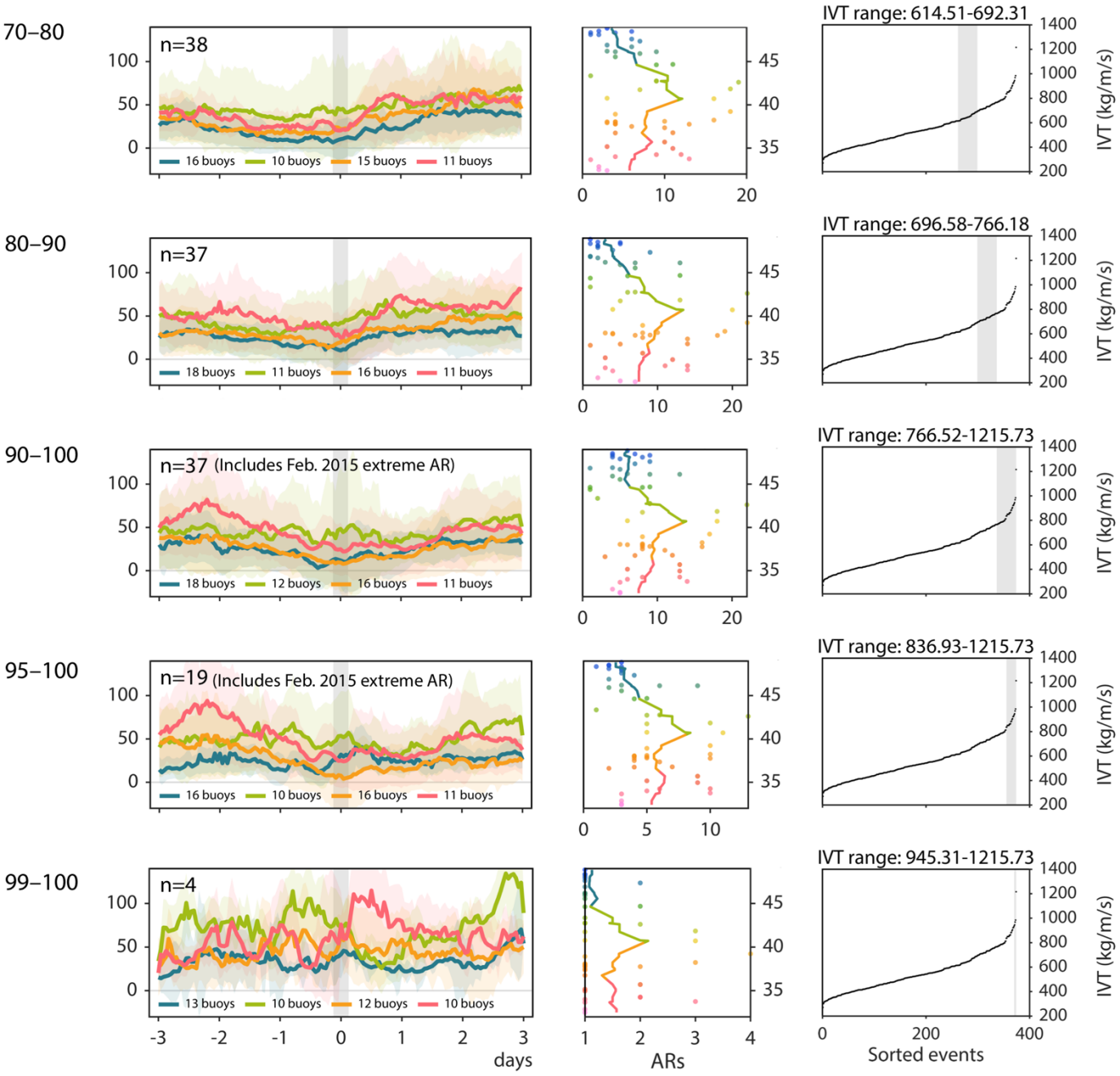

Figure S4. Composite evolution of LHF during ARs, grouped by intensity. ARs are sorted by intensity (maximum IVT during each AR's landfalling lifetime), and composites are performed for each intensity decile, and the 95th and 99th percentile groups, shown as each row. The left two columns are as in Figure 2; the right column shows the intensity of all sorted events (dots), consistent for each row, and indicates the range of intensities within each composite (gray shading). The sample size of ARs for each composite is shown in the upper left corner of each row in the left column. The dotted gray line between deciles 4 and 5 illustrates the lower bound of intensity for ARs considered in the composites in Figure 2. The February 2015 case study extreme AR is >95th percentile intensity, so it is represented in the 10th decile and 95th percentile composites.

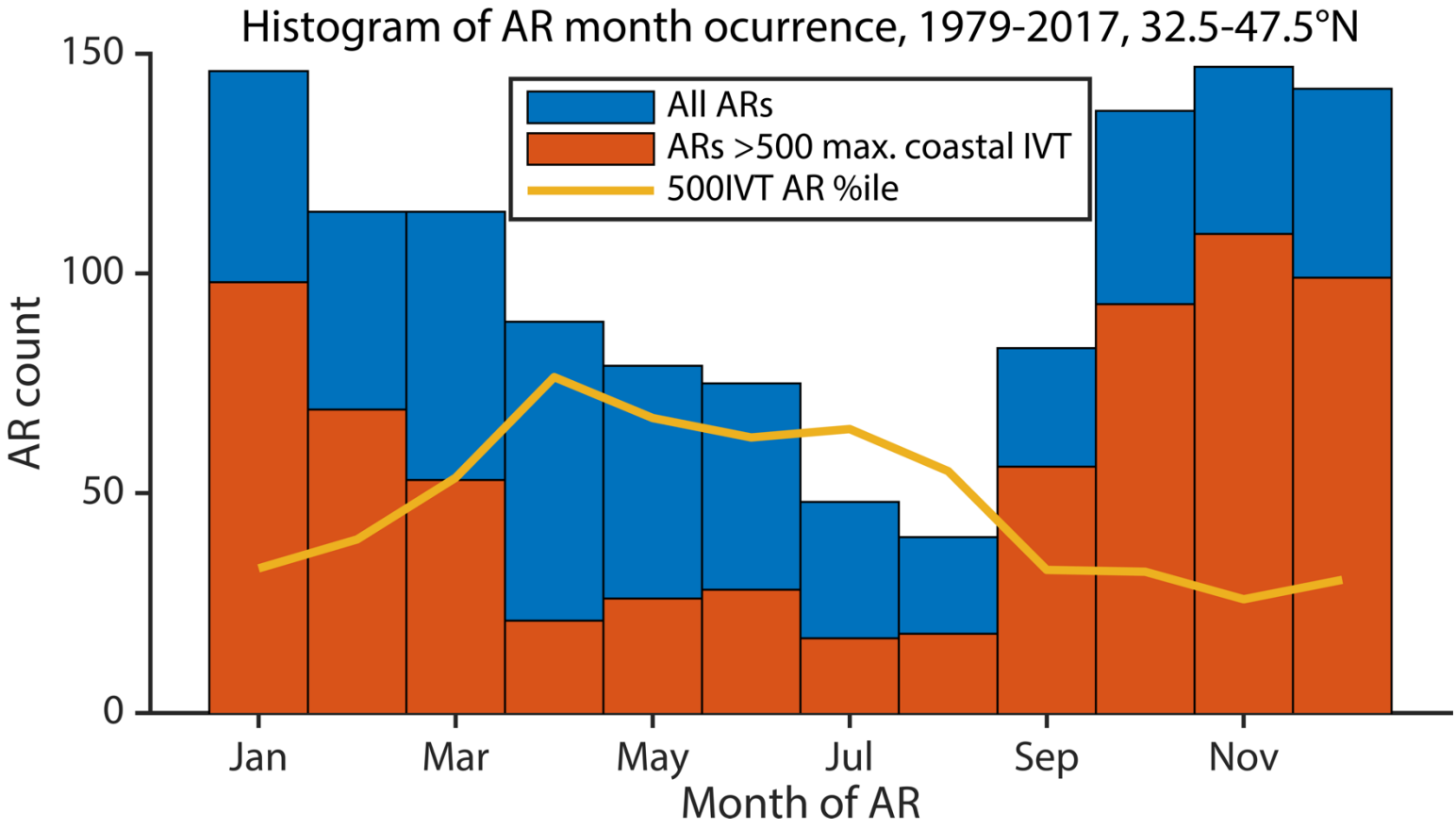

Figure S5. Histogram of AR occurrence in each month of the year, for ARs impacting the U.S. coastline in 1979–2017. Blue bars show the count of ARs of all intensities (at least 250 kg/m/s, according to SIO-R1) in each month, and orange bars show the count of only ARs with lifetime maximum IVT exceeding 500 kg/m/s. The yellow line indicates the intensity percentile of ARs that the 500 IVT threshold represents, and uses the same *y*-axis (from 0–100, in %). In other words the whole-year, November–March, and January–March averages of the yellow line are indicated in the legend of Figure S2. Thus, this figure assesses the variable impact of the 500 kg/m/s intensity threshold for composites of differing month ranges.

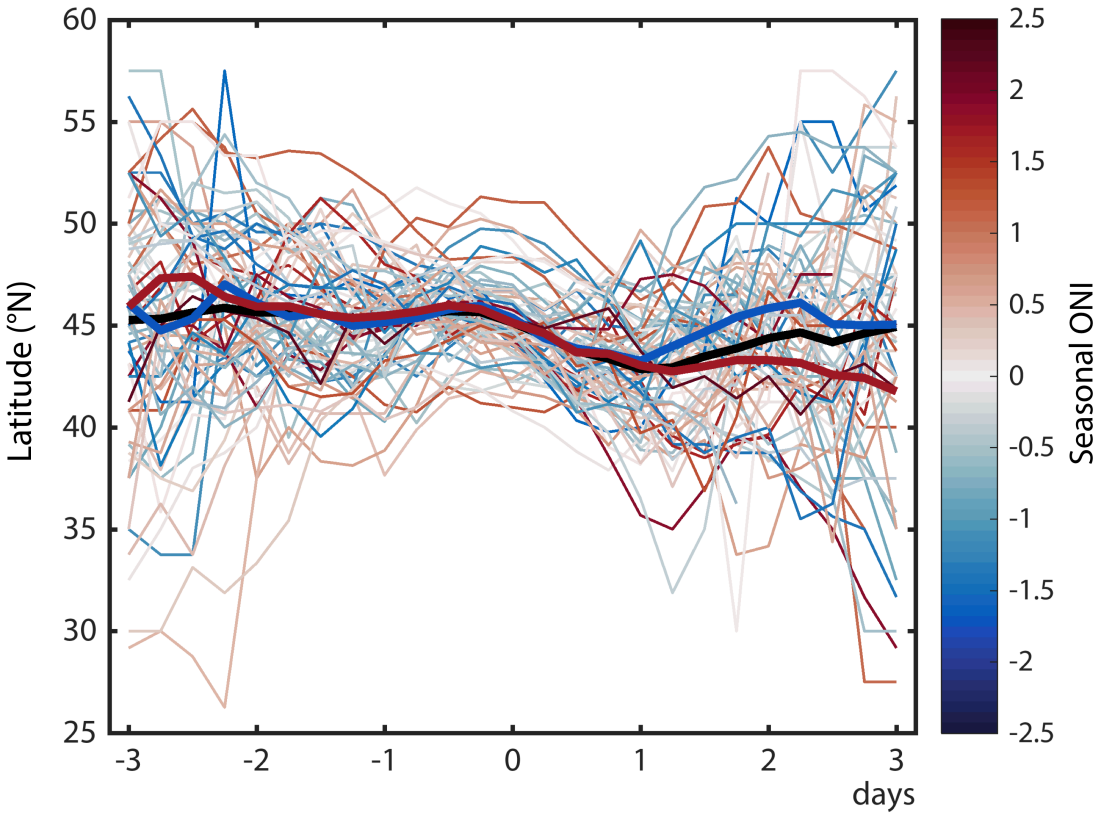

Figure S6: JFM-average AR latitudinal trajectories according to the ENSO phase. Each line tracks the composite evolution of the latitude of maximum along-coastline IVT (i.e., 'landfalling latitude') during all ARs in each JFM 1950–2016 (data from SIO-R1). The color indicates the JFM-averaged ONI for each year. The thick red and blue lines show average trajectories for all El Niño (ONI>0.5) and La Niña (ONI<–0.5) winters, and the thick black line indicates the whole-period average trajectory. This plot considers all JFM ARs available in SIO-R1, extending along the whole North American west coast from 20–60°N (i.e., not restricted to ARs passing near a buoy along the U.S. coast, 32–49°N).

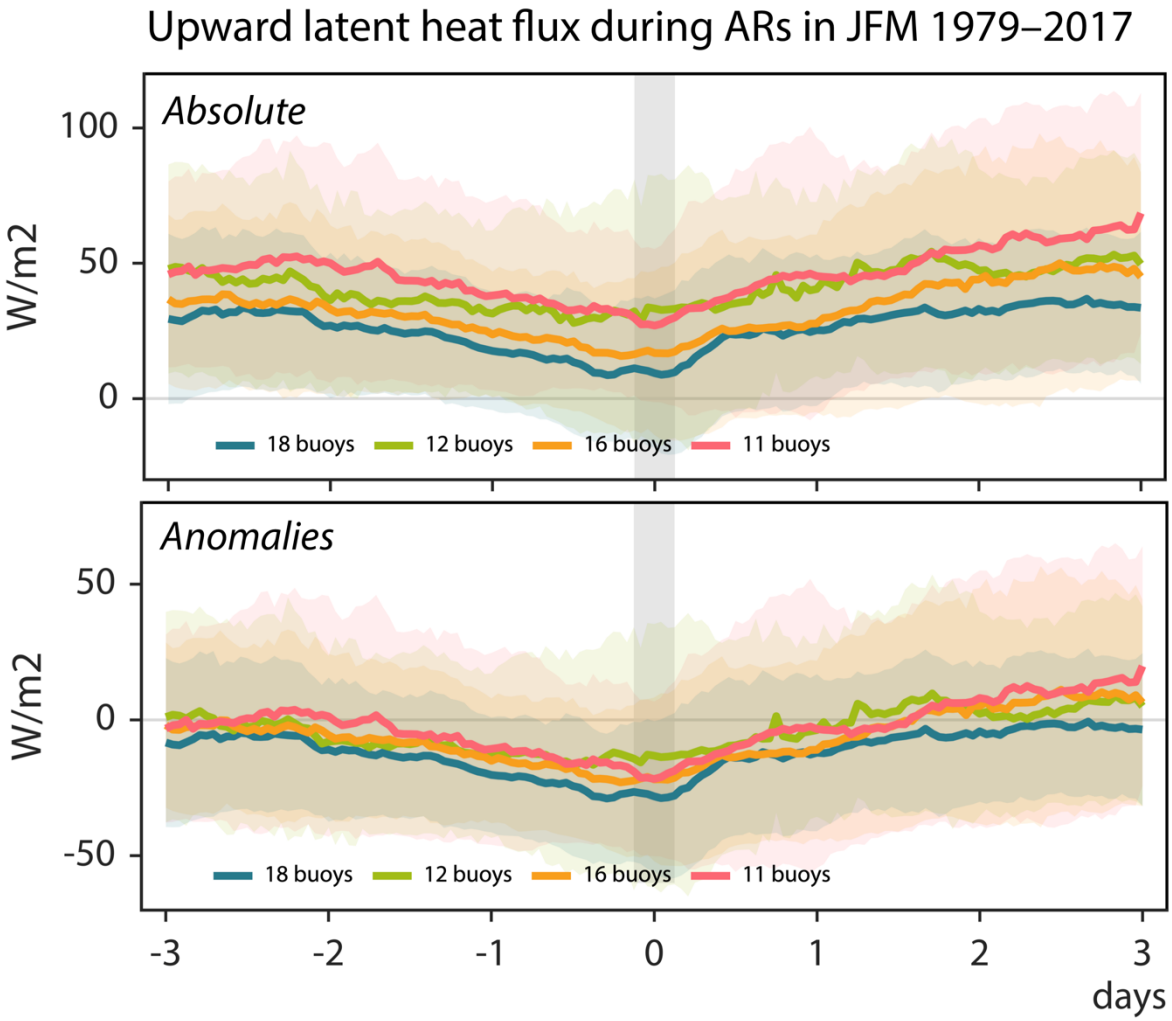

Figure S7. Comparison of absolute vs. anomalous latent heat flux composites during landfalling ARs in late-winter 1979–2017. The top panel is the composite shown in Figure 2f. The bottom panel shows latent heat flux anomalies, i.e., the top panel with each buoy's latent heat flux climatology subtracted. Monthly climatologies (spline-interpolated to hourly) are calculated for all years that each buoy operates.

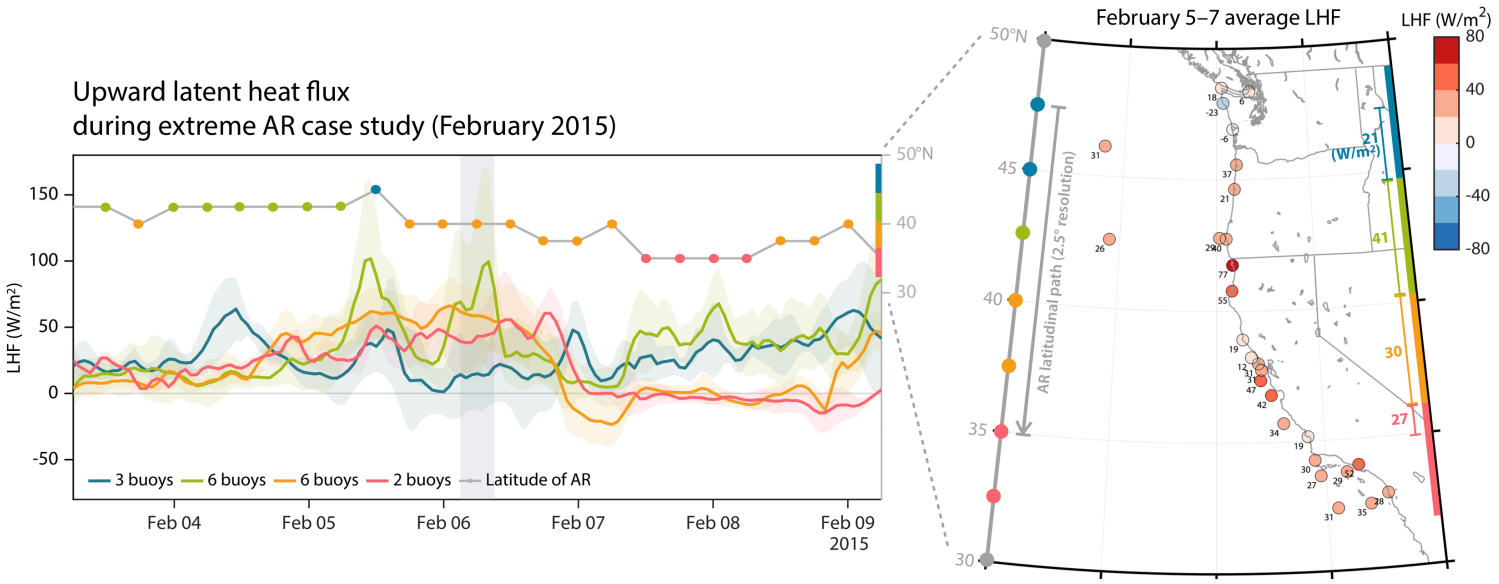

Figure S8. Coastal upward LHF during an extreme AR, and the AR's latitudinal path. Left panel: Using the left *y*-axis, colored lines show latitudinal bin averages of (absolute) upward LHF, derived from buoys and ERA5. Colored shading indicates ±one instantaneous standard deviation around each bin average. The time window is ±3 days centered around the 6-hourly timestep of maximum IVT along the US coastline during the AR (gray vertical shading), from SIO-R1. Using the right *y*-axis, the gray line shows the latitude of maximum IVT at each 6-hourly timestep during the AR (at the 2.5° horizontal resolution of SIO-R1), with markers colored according to the bin containing each latitude. The right *y*-axis also illustrates the extents of buoys' latitudinal bins (colored rectangles). Right panel: The left *y*-axis displays the 2.5° resolution latitudes of SIO-R1, colored according to their bin, and a schematic representation of the AR's latitudinal path (gray arrow). In the interior of the plot, blue-to-red colored dots show LHF averaged throughout February 5–7 at buoys along the shore, with labels specifying precise values. The right *y*-axis shows Feb 5–7-averaged LHF averaged across buoys in each bin, including only buoys within the AR's latitudinal extent. It also illustrates the full extents of buoys' latitudinal bins as in the right *y*-axis of the left panel.

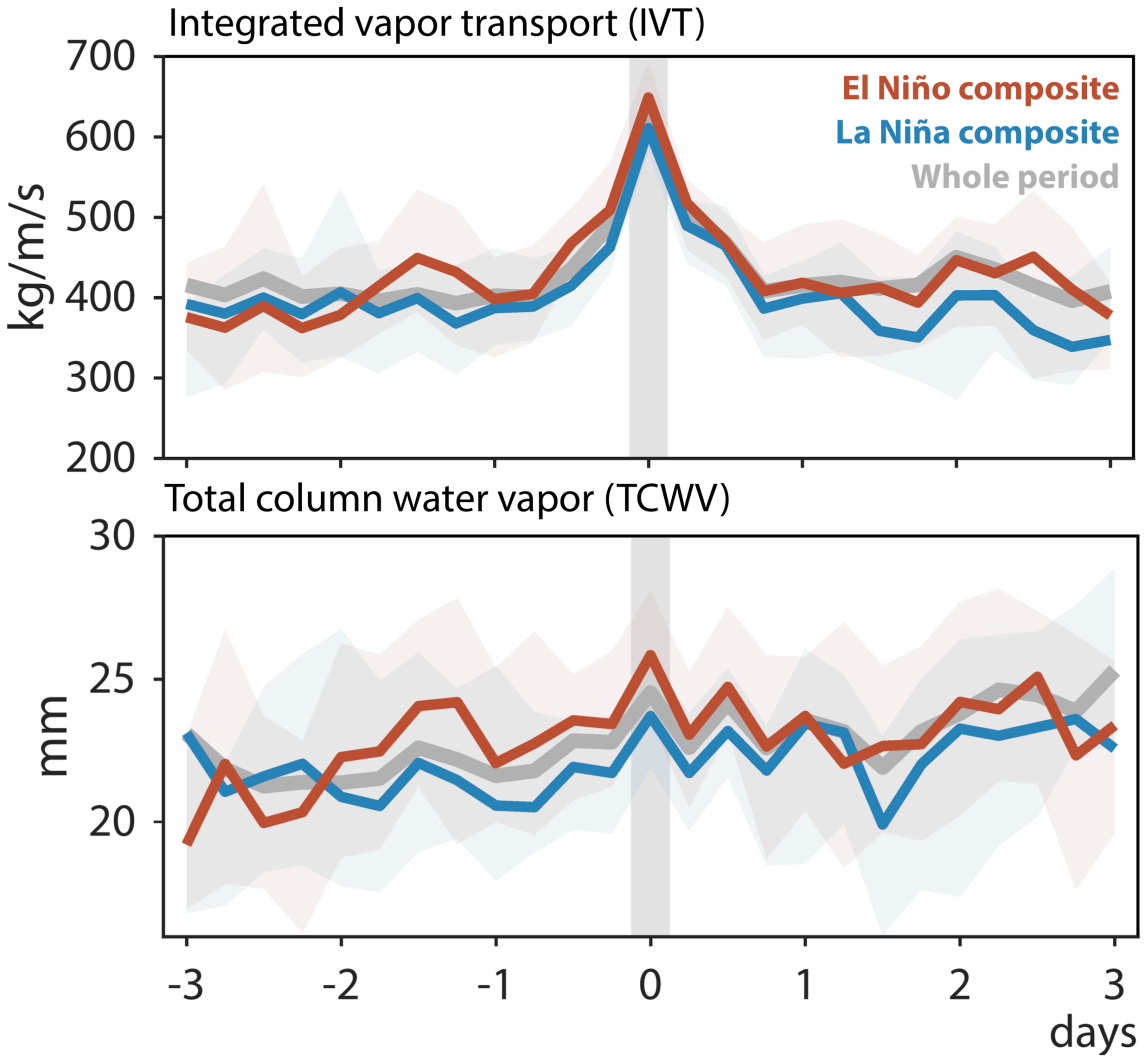

Figure S9. ENSO-phase AR intensity comparisons, with a more restrictive period and event threshold. As in Figure 3's bottom two panels, but only considering ARs in 1979–2017 and with peak IVT exceeding 500 kg/m/s.

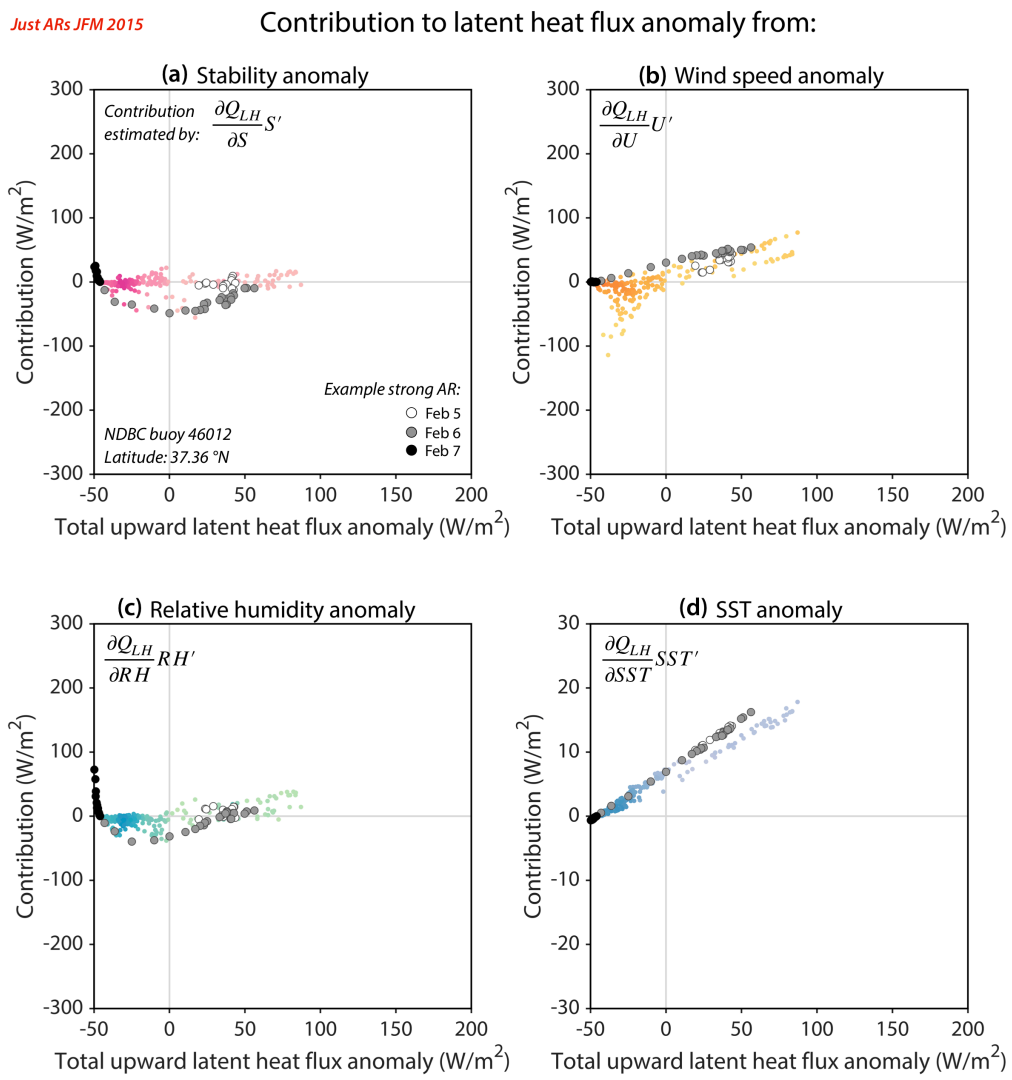

Figure S10. Contribution to LHF anomaly from its constituent variables during ARs affecting NDBC buoy 46012 in JFM2015. As in Figure 4a–d, but for a subset of hours during which an AR was present near NDBC buoy 46012 (within ±5° latitude; 3 ARs included). This relaxes the 500 kg/m/s event intensity threshold used for Figure 2 and elsewhere in the analysis (i.e., includes ARs with maximum IVT between 250 kg/m/s and 500 kg/m/s).

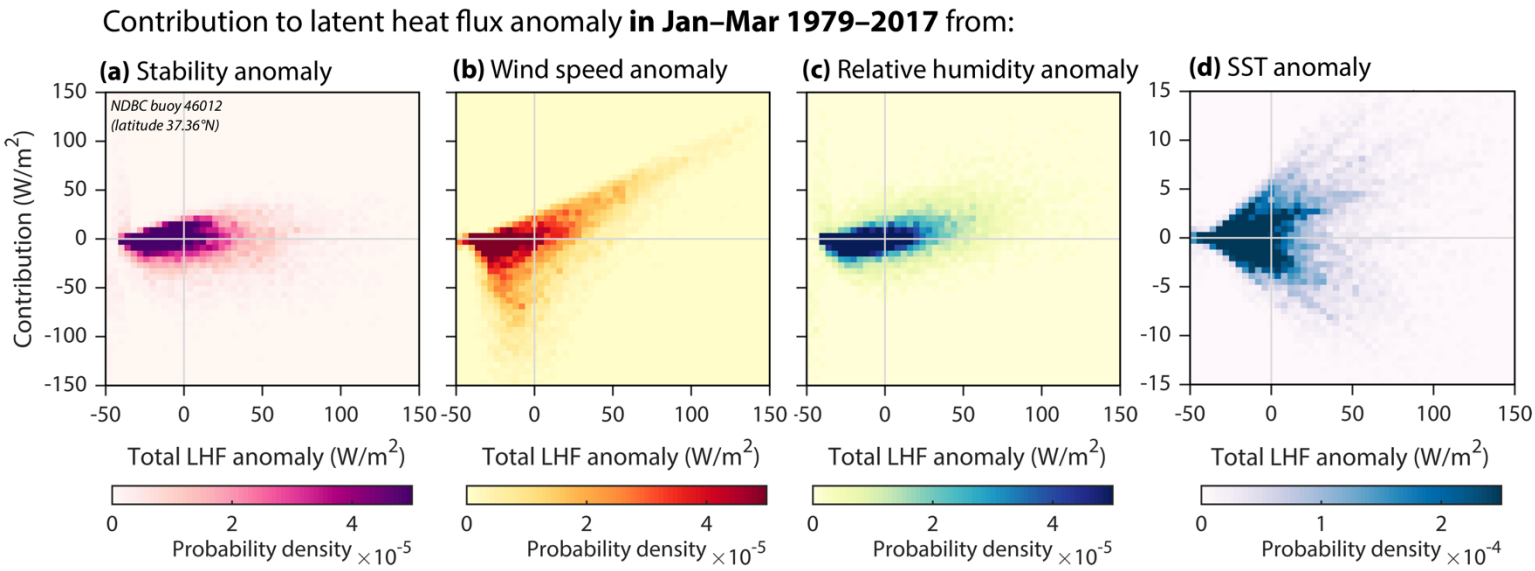

Figure S11. Contributions from constituent variables to latent heat flux at NDBC Buoy 46012, over all late winters (January–March) 1979–2017. This is an all-year version of Figure 4a-d, with hourly contributions shown as 2-d probability distributions (plotted against hourly total latent heat flux anomaly), instead of scattered discrete points. The *y*-axes cover half the range of Figure 4a-d to better visualize the probability distributions. Again, the *y*-axis for SST contribution is 10x smaller than for the other variables. The distributions largely mirror the scatters in Figure 4a-d. In Figure 4, which examined JFM 2015, the SST contributions had remained positive, likely because 2015 was a strong El Niño year. Here, where both El Niño and La Niña years are represented in the time range, the distribution of SST's LHF contributions spreads quasi-symmetrically around zero.

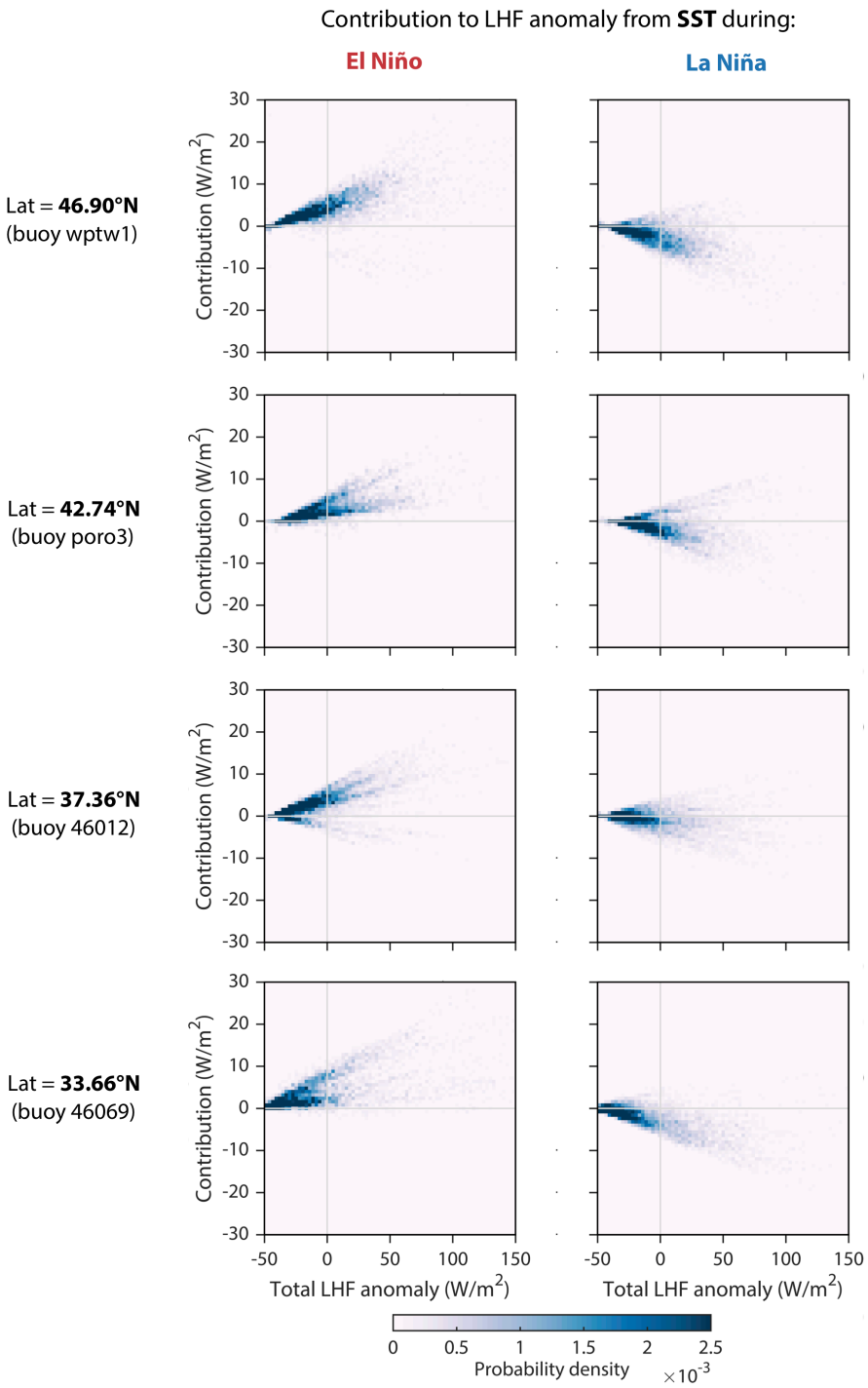

Figure S12. Contribution of SST anomalies to total LHF anomalies, composited by the different ENSO phases. For four example buoys (one in each latitudinal bin shown in Figure 2), the total LHF anomaly (*x*-axis) is plotted against SST anomalies' contribution to that total (*y*-axis) as in Figure 4. Color intensity indicates dot density based on hourly-averaged data. The left column shows data from El Niño late-winters (JFM); the right shows the same for La Niña. These distributions are collapsed along the *x* dimension (retaining only "contribution" information) and shown individually and as a 4-buoy average in Figure 4h.

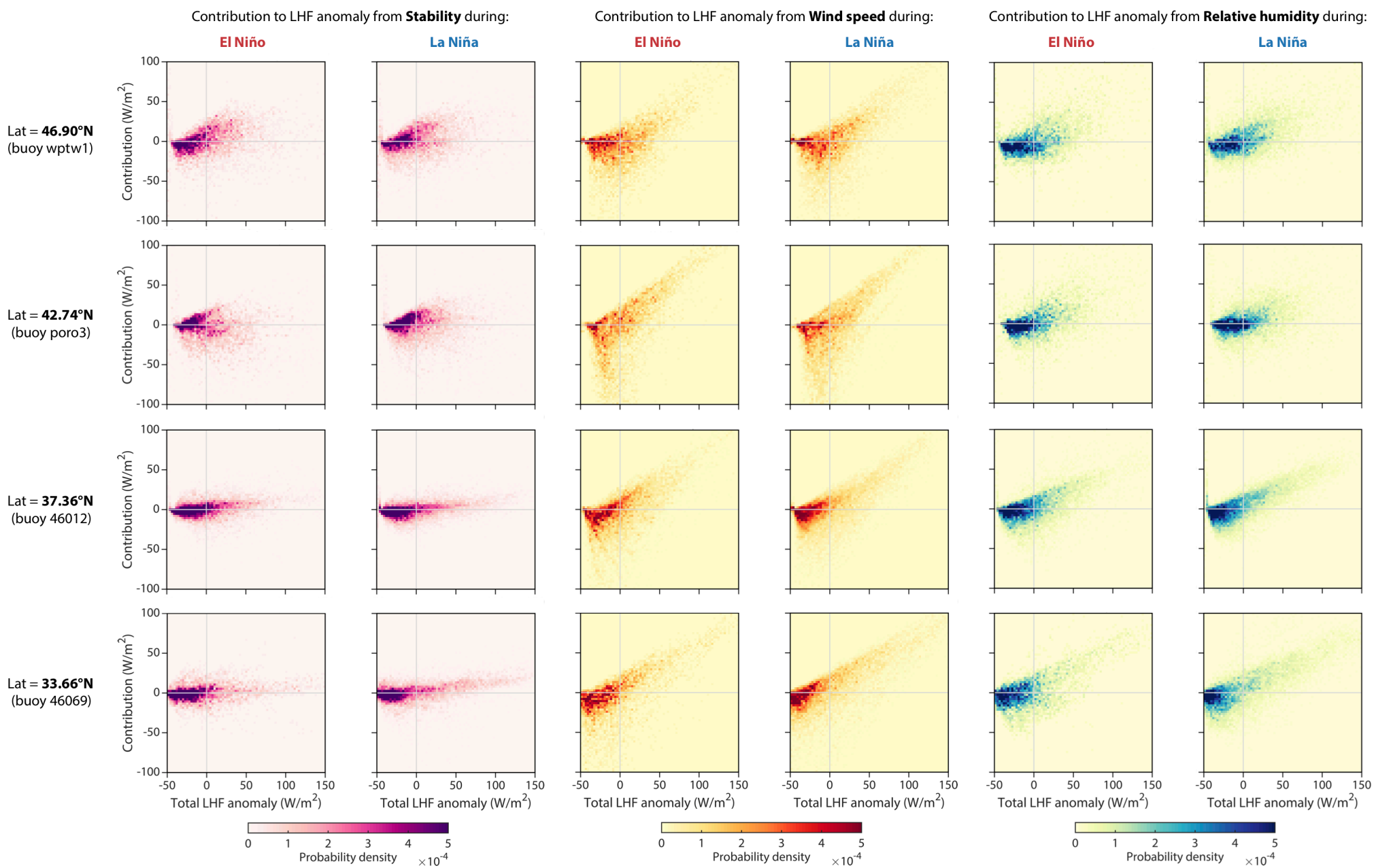

Figure S13. Contribution of wind speed, stability, and relative humidity anomalies toward total LHF anomalies, composited by the different ENSO phases. As in Figure S12, but for near-surface stability, wind speed, and relative humidity, with El Niño and La Niña winters in separate columns for each variable. These distributions are again collapsed along the *x* dimension (retaining only "contribution" information) and, for each variable, shown individually and as 4-buoy averages in Figure 4e-g.